Differences in composition of chromites from low-Ti and high-Ti picrites of the Emeishan Large Igneous Province and comparison with chromites of the UG-2 platinum-deposit of the Bushveld Complex.

Sarah-Jane Barnes*[1], Eduardo T Mansur[1,2], Philippe Pagé [1,3]

[1]Sciences de la Terre, Université du Québec à Chicoutimi, 555 boulevard de l'université, Québec G7H 2B1, Canada

[2]Geological Survey of Norway, P.O. Box 6315 Torgarden, NO-7491 Trondheim

[3] IOS Services Géoscientifiques Inc, 1319 Saint-Paul boul., Chicoutimi G7J 3Y2, Canada

*Corresponding Author

e-mail: sjbarnes@uqac.ca

Keywords: Chromite, trace elements, Emeishan, picrite, UG-2, Platinum-group element ore deposits.

Published as

Barnes, S.-J., Mansur, E.T., Pagé, P., 2022. Differences in composition of chromites from low-Ti and high-Ti picrites of the Emeishan Large Igneous Province and comparison with chromites of the UG-2 platinum-deposit of the Bushveld complex. Lithos 412-413, 106613. https://doi.org/10.1016/j.lithos.2022.106613

ABSTRACT

Chromite is among the first minerals to crystallize from mantle derived magmas and one of the last to be consumed during partial melting of the mantle. Chromite is also an important mineral in major ore deposits of Cr and Pt. The composition of chromite could, therefore be of use in interpreting the petrogenetic conditions during partial melting of the mantle, crystallization of primitive magmas and formation of Pt and Cr ore deposits. However, most mafic rocks contain very little chromite and post-crystallization processes such as re-equilibration during cooling, metamorphism and weathering could change the composition. The composition of chromites from high- and low-Ti picrites from the Emeishan large igneous province have been determined to assess the degree to which the chromite compositions reflect the melt compositions. Aluminium, Sc, Ti, Ga, Nb, Sn, Hf and Ta concentrations in the chromites do appear to reflect the melt compositions in that they correlate with the whole rock compositions and have empirical partition coefficients similar to those determined in experiments. The V contents of both types of picrite are similar, but concentrations of chromites from high-Ti picrites are higher than those of low-Ti picrites. This can be explained if, in the high-Ti picrite more of the V was in the V3+ state (which can more readily substitute into chromite than V4+ or V5+) than in the low-Ti picrite. This implies that fO_2 was lower for high-Ti picrites than low-Ti picrites. Concentrations of elements with a 2+ charge, Mg, Mn, Fe, Co, Ni and Zn are different in chromites included in olivine and chromites in the matrix and appear to have re-equilbrated. The compositions of the UG-2 chromites from the World's largest Pt deposit show some similarities with the chromites from the high-Ti picrite, but are depleted in Sc and Ti and enriched in Ga and Al.

Highlights.

Trace element contents of chromites from Emeishan picrites reflect magma composition

V concentrations controlled by fO_2, low-Ti picrites have higher fO_2 than high-Ti

Concentrations of elements with 2+ charge affected by subsolidus processes.

Composition of chromites from UG2 Pt ore are similar to high-Ti picrite chromites.

Differences in composition of chromites from low-Ti and high-Ti picrites of the Emeishan Large Igneous Province and comparison with chromites of the UG-2 platinum-deposit of the Bushveld Complex.

Sarah-Jane Barnes*[1], Eduardo T Mansur[1,2], Philippe Pagé [1,3]

[1]Sciences de la Terre, Université du Québec à Chicoutimi, 555 boulevard de l'université, Québec G7H 2B1, Canada

[2]Geological Survey of Norway, P.O. Box 6315 Torgarden, NO-7491 Trondheim

[3] IOS Services Géoscientifiques Inc, 1319 Saint-Paul boul., Chicoutimi G7J 3Y2, Canada

*Corresponding Author

e-mail: sjbarnes@uqac.ca

Keywords: Chromite, trace elements, Emeishan, picrite, UG-2, Platinum-group element ore deposits.

ABSTRACT

Chromite is among the first minerals to crystallize from mantle derived magmas and one of the last to be consumed during partial melting of the mantle. Chromite is also an important mineral in major ore deposits of Cr and Pt. The composition of chromite could, therefore be of use in interpreting the petrogenetic conditions during partial melting of the mantle, crystallization of primitive magmas and formation of Pt and Cr ore deposits. However, most mafic rocks contain very little chromite and post-crystallization processes such as re-equilibration during cooling, metamorphism and weathering could change the composition. The composition of chromites from high- and low-Ti picrites from the Emeishan large igneous province have been determined to assess the degree to which the chromite compositions reflect the melt compositions. Aluminium, Sc, Ti, Ga, Nb, Sn, Hf and Ta concentrations in the chromites do appear to reflect the melt compositions in that they correlate with the whole rock compositions and have empirical partition coefficients similar to those determined in experiments. The V contents of both types of picrite are similar, but concentrations of chromites from high-Ti picrites are higher than those of low-Ti picrites. This can be explained if, in the high-Ti picrite more of the V was in the V3+ state (which can more readily substitute into chromite than V4+ or V5+) than in the low-Ti picrite. This implies that fO_2 was lower for high-Ti picrites than low-Ti picrites. Concentrations of elements with a 2+ charge, Mg, Mn, Fe, Co, Ni and Zn are different in chromites included in olivine and chromites in the matrix and appear to have re-equilbrated. The compositions of the UG-2 chromites from the World's largest Pt deposit show some similarities with the chromites from the high-Ti picrite, but are depleted in Sc and Ti and enriched in Ga and Al.

1. Introduction

The advent of laser ablation inductively coupled plasma-mass spectrometry (LA-ICP-MS) analyses has opened the opportunity to document trace element concentrations in minerals down to ppm or even ppb level. These observations have been used in petrogenetic studies and for mineral exploration. Chromite is of particular interest. In the case of petrogenetic studies, it of interest because it appears early in the crystallization of mantle derived magmas and is one of the last minerals to be consumed during partial melting of the mantle. Consequently, there are numerous recent studies of trace elements in chromites from rocks representing mantle fragments, ophiolites and nodules, with aim of establishing the type of magma that the chromite crystallized from (Pagé and Barnes, 2009; Gonzalez-Jimenez et al., 2014; Zhou et al., 2014. Chromite from komatiite has also been studied to document the oxygen fugacity of the early earth (Canil, 2002; Nicklas et al., 2016. In addition, Kamenetsky et al. (2001) proposed a plot of TiO_2 vs Al_2O_3 to distinguish chromites from volcanic rocks of various tectonic settings.

The trace element content of chromites is also of interest in exploration for ore deposits. For example, the concentration of Ru in chromite has been proposed as an exploration technique (Locmellis et al., 2011). The largest platinum-group element (PGE) deposit in the world, the UG-2, of the Bushveld Complex consists of massive chromitite layers (Naldrett et al., 2012). Platinum deposits are also found in association with chromitites from zoned complexes of the Urals (Garuti et al., 2012) and British Columbia (Nixon et al., 1990). Possibly the trace element content of the chromites from different settings are different and could be used in exploration programs. On the petrogenetic side it might be possible to deduce the composition of the magmas from which chromite crystallized and thus help in understanding how the ores form. However, before this can be accomplished, it is necessary to establish to whether trace element contents of chromite record the composition of the melt from which they crystallized.

Many of the large Ni-Cu-PGE deposits (Bushveld and Stillwater Complexes, the Great Dyke and Noril'sk-Talnakh) are thought to have formed either from komatiite magmas or picrites contaminated with continental crust material (Barnes et al., 2010; Wilson et al., 2012; Maier et al., 2016; Jenkins and Mungall, 2018; Latyshev et al., 2020; Tolstykh et al., 2020; Solovova et al., 2021). In the current study we assess whether chromite compositions are representative of the magma compositions by examining the compositions of chromite grains from both high- and low-Ti picrites from the Emeishan Large Igneous Province (LIP) of China. The low-Ti and high-Ti picrite melts have different Al, Ti, Fe, Nb, Sn, Hf and Ta concentrations. We show that this difference is reflected in the chromite compositions except for Fe. We also show that the composition of the chromite grains is influenced by their habit. Chromite grains occur in two main habits - enclosed in olivine phenocrysts (hereafter referred to as inclusion chromites) and in the fine-grained matrixes (hereafter referred to as matrix chromites). The concentrations of Al, Sc, Ti, V, Ga, Nb, Sn, Hf and Ta are the similar for both types of grain. Whereas inclusion chromite are richer in MgO and Co and poorer in FeO, MnO and Zn than matrix chromites. We also show that the trace elements in chromites from the high Ti-picrites show some similarities with the trace elements content of the UG-2 chromites.

2. Geological Setting.

The Emeishan LIP province occurs in south-western China covering an area of > 250,000 km^2 in the Yunnan, Sichuan and Guizhou Provinces, for a total volume of 0.3×10^6 km^3 (Ali et al., 2005).The lavas were emplaced over a short period 1–2 Ma; Ali et al., 2005) at around 260 Ma. The lava sequence ranges in thickness from 1000 to more than 5000 m in the western part of the province, and from 200 to 2600 m in the eastern part (Shellnutt, 2014) and consists mostly of tholeiitic basalts which represent more than 95% of the magma volume (Xiao et al., 2004;

Hanski et al., 2010). Picrites are mainly found in the western part of the province (Song et al., 2001; Xu et al., 2001; Xiao et al., 2004; Zhang et al., 2005, 2006; Hanski et al., 2010) and in the Jinping area in southern Yunnan Province close to the China–Vietnam border (Wang et al., 2007). The Emeishan picritic flows are mainly observed in the lower and middle parts of the volcanic sequences and can reach several tens of metres in thickness (Xu et al., 2001; Xiao et al., 2004; Zhang et al., 2005, 2006, 2008).

In addition to the volcanic rocks, the Emeishan LIP also contains intrusive rocks including numerous mafic to ultramafic dikes and intrusions which are mainly exposed in the Panxi region due to several N–S-trending faults (Zhou et al., 2008. Two main types of mineral deposits are present: 1) Ni–Cu–(PGE) sulfide deposits; and 2) Fe–Ti–V oxide deposits. The magmatic sulfide deposits are found mainly in small, primitive intrusions throughout the entire flood basalt province. They include Ni–Cu–(PGE) sulfide deposits hosted by mafic–ultramafic intrusions (Song et al., 2003, 2004, 2006; Wang and Zhou, 2011; Wang et al., 2006; Tao et al., 2010) and PGE mineralization within ultramafic rocks (Jinbaoshan: Wang et al., 2005, 2008; Tao et al., 2007). In contrast, the Fe–Ti–V oxide deposits occur in larger and more evolved intrusions which are mainly distributed in the Panxi region along major N–S-trending faults (e.g. Taihe, Xinjie, Baima, Hongge and Panzhihua: Zhou et al., 2005, 2008, 2013; Zhong and Zhu, 2006, Chen et al., 2017).

Based mainly on their Ti/Y ratios, Xu et al. (2001) classified the tholeiitic basalts into low-Ti basalts which have Ti/Y < 500, and high-Ti basalts with Ti/Y > 500. Zhou et al. (2013) proposed that the mafic–ultramafic intrusions that host the Fe–Ti–V oxide deposits were formed from high-Ti basalts, whereas the Ni–Cu sulfide-bearing intrusions are genetically associated with the low-Ti magma series.

3. Materials and Methods

The samples used in this study were previously studied by Arguin et al. (2016) who investigated the role chromite plays in controlling PGE. The samples are fresh to slightly weathered picrites and were collected mainly from road cuts in four locations: Dali, Binchuan, Jianchuan and Lijiang, in the western part of the Emeishan LIP (Fig. 1). The Lijiang area includes the Shiman and Daju lavas. In addition, three samples from a subvolcanic sill from the Ertan area, close to Panzhihua (Sichuan Province), were also included. The UTM co-ordinates for each sample are provided in Electronic Supplementary Material (ESM1 Table 1). In general, the outcrops where samples were collected are moderately to highly weathered due to a subtropical monsoon climate. Care was taken to collect samples from the preserved parts of the outcrops.

Samples were crushed in a steel jaw crusher and then pulverized in Al-ceramic shatter box at LabMaTer, Université du Québec à Chicoutimi (UQAC). The whole rocks were analyzed for major oxides, by X-ray fluorescence, and for trace elements, ICP-MS on solutions obtained, after the powders had been dissolved by four acids in a closed vessel, at Geoscience Laboratories, Sudbury. Reference materials (ESM 1 Table 2) were analyzed in the same batch and the results agree with working values. Individual whole-rock compositions recalculated to 100% anhydrous are listed in (ESM 1 Table 3) and averages are shown in Table 1.

Polished thin sections (30 μm thick) were made of each sample. These were examined with a petrographic microscope and chromite grains were selected for *in situ* analysis. The major elements were determined on a CAMECA SX100 microprobe with wavelength dispersive spectrometry at the Université Laval, Québec City. These results have been previously reported by Arguin et al. (2016). The average analyses are reported in Table 2.

The concentration of major minor and trace elements in chromite were determined by LA-ICP-MS at LabMaTer using an Excimer 193 nm RESOlution M-50 laser ablation system (Australian Scientific Instrument) equipped with a double volume cell S-155 (Laurin Technic) and coupled with an Agilent 7900 mass spectrometer. The LA-ICP-MS tuning parameters were a laser frequency of 10 Hz, a power of 3 mJ/pulse, a dwell time of 7.5 ms, a rastering speed of 5 to 10 μm/s, and a fluence of 5 J/cm^2. Line scans across the surface of grains were made with beam sizes of 55 or 44 μm, depending on grain size. The gas blank was measured for 30s before switching on the laser for around 60s. The ablated material was carried into the ICP-MS by an Ar–He gas mix at a rate of 0.8–1 L/min for Ar and 350 mL/min for He, and 2mL/min of nitrogen was also added to the mixture. Data reduction was carried out using the Iolite package for Igor Pro software (Paton et al., 2011). Maps of the element distribution were made of some chromite grains using the same parameters with various stage movement speeds to optimize spatial resolution and analysis time of the areas being mapped. The maps were generated using the Iolite package based on the time-resolved composition of each element. The maps indicate the relative concentration of the elements and are semi-quantitative.

The isotopes ^{29}Si, ^{44}Ca, ^{31}P, ^{33}S, ^{75}As, ^{121}Sb, ^{209}Bi, were monitored in order to exclude inclusions of; silicate, carbonate, apatite and sulfide minerals. Inclusions were rare and excluded from the analyses. The isotopes ^{24}Mg, ^{27}Al, ^{45} Sc, ^{49}Ti, ^{51}V, ^{52}Cr, ^{55}Mn, ^{57}Fe, ^{59}Co, ^{60}Ni, ^{63}Cu, ^{66}Zn, ^{71}Ga, ^{89}Y, ^{93}Nb, ^{95}Mo ^{101}Ru, ^{103}Rh, ^{108}Pd, ^{111}Cd, ^{115}In, ^{118}Sn, ^{178}Hf, ^{181}Ta, ^{185}Re, ^{189}Os, ^{193}Ir, ^{195}Pt, ^{197}Au were used to determine the concentrations of these elements. The possibility of interference of ^{53}Cr^{40}Ar on ^{93}Nb was investigated. However, there appears to be no correlation between Cr and Nb, for example Nb concentrations in the in house reference chromites AX37 and MIA which contain 55 and 60 weight percent respectively Cr_2O_3 are 0.015 ppm (close to

detection limit). Hence the Cr interference on Nb was considered negligible. The concentrations of Sn are too low for ^{115}Sn to produce a significant interference on ^{115}In, and were ignored.

External calibration was carried out using three reference materials. GSE-1g with a composition close to a basaltic glass and doped with ~400 ppm of most trace elements supplied by USGS was used for minor and trace elements, except the PGE, Au and S. Laflamme Po727 a FeS dopped with ~ 40 ppm of each PGE and Au was used for the PGE and Au. A natural chromite, M1A (mantle chromite from the Thetford ophiolite) was used for the major elements Al, Mg and Cr. ^{57}Fe was used for internal calibration. Natural chromites from two in-house reference materials AX 37 (a komatiite) and M1A (ophiolite), and GProbe 6, a basaltic glass were used as monitors. The results obtained for the monitors agree within analytical error with the working values (ESM 1, Table 4). Averages obtained for the Emeishan chromites by LA-ICP-MS are reported in Table 3 a full list is available in (ESM 1, Table 5).

4. Results and Interpretation

4.1 Petrography

The picrites have a porphyritic texture and contain 10 to 45% (modal) phenocrysts of olivine (0.2 to 10 mm) in a fine grained (<0.1 mm) matrix of clinopyroxene, plagioclase, oxide and devitrified glass (Fig 2a of Arguin et al., 2016). Chromite (0.05 to 0.8 mm) is present in a small amounts (<1% modal) in three habits: a) as inclusions in the olivine phenocrysts, (Fig. 2a); b) as isolated grains in the matrix (Fig. 3a), and c) at the contact between the olivine phenocrysts (Fig. 2b of Arguin et al., 2016.

The olivine is euhedral to sub-euhedral with a narrow (<0.1 mm) rim with difference in birefringence colors indicating a sharp compositional change. Microprobe analyses show that the olivine phenocrysts compositions range from Fo_{84} to Fo_{88} in the high-Ti picrites and Fo_{86} to Fo_{92}

in the low Ti-picrites (Arguin et al., 2016) similar to the range previously reported from the Emeishan picrites (Kamenetsky et al., 2012). The rims show sharply lower Fo contents (Arguin et al., 2016). Some of the olivine grains have been variably serpentinized.

The inclusion chromites are euhedral with sharp boundaries with olivine (Fig. 2). Maps of the major and trace element distribution made by LA-ICP-MS show that the grains and are compositionally unzoned (Fig. 2), except for Cu. There is appears to be, a narrow rim of Cu enrichment at the margins of the grains (<10 μm). The chromites in the matrix are also euhedral but have narrow (<0.05 mm) titano-magnetite overgrowths (Fig. 3). The matrix chromites are unzoned, except as in the case of the inclusion chromites, there is a narrow rim enriched in Cu. The titano-magnetite rims are enriched in Ti, V, Mn, Fe, Ni, Zn, Nb, Sn and Hf, these rims were excluded from the chromite analyses.

4.2 Whole rock Composition.

Due to the presence of the olivine and chromite phenocrysts the whole rock compositions of the picrites do not represent the composition of the melt. The whole rock compositions represent a mixture of olivine + chromite and transporting melt. Based on melt inclusions in olivine Hanski et al. (2010) and Kamenetsky et al. (2012) estimated highest the MgO content of parental liquids in the Emeishan picrites to be approximately 18 weight percent MgO for the high-Ti picrites and 21 weight percent for the low-Ti picrites. Based on the highest Fo contents of the olivine, Hanski et al. (2010) estimated the highest MgO contents of the parental liquids to be from 20 to 23 weight percent. Based on the highest Fo contents of the olivine observed in our sample set, Arguin et al. (2016) estimated the MgO content of the most primitive parental liquids to be 21 weight percent for low Ti picrites, and 18 weight percent for the high-Ti picrite.

For the purposes of characterizing the chromites, our work will concentrate only on the whole-rock distribution of the elements that can be determined in chromite. Nickel and Co show positive correlations with MgO, whereas FeO_T (all Fe expressed as FeO), MnO and Zn concentrations do not change with MgO content (Fig. 4a to e). These observations are consistent with the partition coefficients for Ni and Co into olivine being higher than 1 and those of Mn and Zn being close to one (Bédard,, 2005). The low-Ti and high-Ti picrites plot along the same lines, except for FeO_T. The high-Ti picrites are richer in FeO_T at a given MgO than the low-Ti picrites.

Chrome also shows a positive correlation with MgO, which is not due to olivine control because; a) the concentration of Cr in olivine (<600 ppm, Arguin et al., 2016) is much lower than that observed in the rocks, and b) the partition coefficient of Cr into olivine for magmas with 12-20 wt % MgO is less than 1 (~0.5 to 0.6, Bédard,, 2005). Both observations indicate that in addition to olivine, chromite has accumulated in the rocks. The regression line through the picrite samples is Cr = 93.5*MgO-13.8. At 47 weight percent MgO (average MgO content of our olivines) there would be 4380 ppm Cr present. The average Cr content of olivine is 550 ppm thus 3850 ppm Cr is in excess. The Cr content of our chromite is on average 322980 ppm. Dividing the excess Cr by Cr content of chromite gives 1.2 weight percent chromite present along with 98.8 percent olivine, which seems reasonable as it is close to cotectic portions (Roeder et al., 2006).

Elements incompatible with olivine; Ti, Al, Sn, Hf, Nb, Ta, V, Cu, Ga (Bédard, 2005) all show negative correlations with MgO (Fig. 5a to f and 6a to c) consistent with olivine fractionation and/or accumulation. These elements may also be divided into those showing differences between the high-Ti picrites and low-Ti picrites; Ti, Al, Sn, Hf, Nb, Ta (Fig. 5a to f, Table 2, and those present at similar levels in both types of picrites Ga, V and Cu (Fig. 6a to c,

Table 2). Titanium, Sn and Hf are present at higher levels and Al at lower levels in high-Ti picrites than in low-Ti picrites (Fig. 5a to d). Niobium and Ta do not behave consistently; the Dali picrites contain less Nb and Ta than the high-Ti picrites, whereas the Binchuan contain similar levels to the high-Ti picrites (Fig. 5e and f). For both types of the picrites Sc does not appear to vary with MgO content and is present at 20 to 30 ppm, although in the basalts it starts to fall, presumably once clinopyroxene crystallizes (Fig. 6d).

To estimate the composition of the transporting melt the olivine and chromite phenocrysts must be subtracted from each sample. This was done by using the average olivine composition found in each sample and subtracting this composition in one weight percent increments from the whole rock composition until the calculated liquid composition was in equilibrium with the olivine of the observed composition, assuming

K_D ($[Mg_{liq}]*[Fe_{ol}]$)/($[Fe_{liq}]*[Mg_{ol}]$) = 0.3 (Roeder and Emslie, 1970.)

This approach required extraction of between 4 and 45 weight percent olivine along with appropriate amount of chromite (0.05 to 0.56 wt%). The calculated MgO concentrations of the transporting magmas ranged from 10 to 20 weight percent (Table 4).

4.3 Chromite Composition

4.3.1 Major Elements

Chromium, Ti, Al, Fe and Mg were determined by both microprobe and LA-ICP-MS. The results for the two methods agree within two relative percent. On the assumption that the probe data are more precise for these elements the probe data will be used, but the conclusions would be similar if the LA-ICP-MS data were used.

The chromites from low-Ti picrites are richer in, Al_2O_3 than the chromites from the high Ti-picrites, which are in turn richer in Al_2O_3 than the chromites from the sill (Table 2, Fig. 7a).

In contrast the Cr_2O_3 of chromites from high- and low-Ti picrites cover a similar range (Fig. 7b) and Table 2. The higher Al_2O_3 content of chromites from high-Ti picrites is consistent with the higher Al_2O_3 content of the low-Ti picrite melt. Barnes and Roeder (2001) observed that chromites from intrusions from flood basalts are generally richer in Al_2O_3 than the chromites from the associated basalts, which also appears to the case for our sill chromites. The range in compositions of the chromite in equilibrium with the low and high-Ti melts (Table 4) have been calculated using SPINMELTS2 (Nikolaev et al., 2018) at 100MPa and fO_2 of ΔFMQ +1 and 0 respectively. (The choice of fO_2 will be justified in the next section). In terms of Ti, Cr and Al the range in observed chromite compositions are similar to the range in calculated chromite compositions in equilibrium with these melts (stars on Fig. 7a and b).

The FeO_T content of the chromites of the high-Ti picrites and sill are higher than the chromites from the low-Ti picrites and correspondingly poorer in MgO (Table 2, Fig. 7c and d). The MgO and FeO_T contents calculated by SPINMELTS2 are systematically higher for MgO and lower for FeO_T than the observed compositions and the observed compositions cover a much wider range. It has long been known that Fe, Mg, Mn and Zn in chromite re-equilibrate with the mafic silicates or trapped liquid (Roeder and Campbell, 1985; Scowen et al., 1991; Barnes, 1998) whereas ions with a larger charge such as Al, Cr, and Ti are less readily disturbed. Possibly the reason for the difference between the calculated and observed chromite compositions for MgO and FeO_T is the result of the 2+ ions having re-equilibrated with olivine in the case of the inclusion chromite and with the melt in the case of the matrix chromite.

The interpretation that Fe and Mg have re-equilibrated whereas Cr, Al and Ti have not is enforced by the observation that the FeO_T and MgO content of the inclusion and matrix chromites are significantly different with inclusion chromites being richer in MgO and poorer in

FeO_T (Table 2, Fig. 8a and ESM 2 Fig 1). In contrast there is no significant difference in Cr_2O_3, Al_2O_3 and TiO_2 contents of inclusion chromites and matrix chromites (Table 2, Fig. 9a and b and ESM 2 Fig. 2). This interpretation is also consistent with the observation that 3+ and 4+ ions diffuse more slowly in chromite than 2+ ions (Coulthard et al., 2021).

4.3.2 Minor and Trace Elements

In a previous LA-ICP-MS study with conditions optimized for the determination of PGE Arguin et al. (2016) reported results for Os, Ir, Ru and Rh. In the current study PGE were also determined (Table 3) and Os, Ir, Ru and Rh found to be present at similar levels to those reported by Arguin et al. (2016). Palladium, Re, Pt and Au concentrations were found to present at less than detection limits of 10 to 30 ppb (Table 3). Molybdenum, Y, Cd, In, W and Bi were also determined, and the results are above detection limits but less than limits of quantification (Table 3). None of the above elements will be considered any further in our study.

The elements that could be quantified by LA-ICP-MS are; Al, Mg, Cr, Fe, Sc, V, Ti, Mn, Co, Ni, Cu, Zn, Ga, Nb, Sn, Hf and Ta. The Al, Mg, Cr and Fe contents of the chromites have been discussed above. Consistent with the whole rock chemistry, the chromites from high-Ti picrites are enriched in Ti, Nb, Sn, Hf, and Ta relative to chromites from the low-Ti picrites (Fig. 10a to e, Table 3). Despite having similar whole rock values for V, the V concentrations in chromites from the low-Ti picrites is generally lower than V concentrations in chromites from the high-Ti picrites (Fig. 10f, Table 3). Manganese, Co, Ni, Zn Sc and Ga contents are similar in chromites from both types of picrites (Fig. 11a to f, Table 3).

There is no significant difference in concentrations of the 3+, 4+ and 5+ ions, Ti, Sc, V, Ga, Nb, Sn and Hf between inclusion chromites and matrix chromites (Table 3, Fig. 9b to f, ESM 2 Fig. 2) . In contrast, some 2+ ions do show differences with inclusion chromites being poorer

in Mn and Zn than matrix chromites and some inclusion chromites from Hi-Ti picrites being enriched in Co (Table 3 Fig. 8c to d). Nickel does not show any significance between inclusion and matrix chromite (ESM 2 Fig. 1b).

Copper concentrations vary widely from 10 ppm to 300 ppm with no systemic pattern. The possibility that the Cu concentrations are an analytical artefact was considered. However, there is no correlation with elements that could potentially interfere with Cu such as Ti. The time-resolved spectra for Cu in chromite grains with high Cu values do not show peaks as might be expected if Cu-rich inclusions were present. In addition, higher Cu values were found both in this LA-ICP-MS study and in the study by Arguin et al. (2016) when the analytical conditions were different. We therefore conclude that Cu is indeed present at up to 300 ppm in some chromite grains. The Cu content of the high and low-Ti picrites are similar at ~ 100 ppm Cu and the chromites from both low-Ti and high-Ti picrites and show similar ranges in Cu thus the composition of the melt does not appear to be important. The presence of Cu enrichment at the edge of the chromite grains observed on the maps (Fig. 2 and 3) may provide an explanation. If the section chromite exposed in the polish section happened to expose mainly the edge of chromite then the time resolved analysis spectrum may appear homogeneous and high. Possibly Cu was present in a boundary layer at the edge of growing chromite and was incorporated in this manner.

4.4 Oxygen fugacity

There is no significant difference in $Fe^{3+}/\Sigma Fe$ of chromite grains from high-Ti picrites and chromite grains from low-Ti picrites (averages 0.26 +/-0.04 and 0.24 +/-0.04 respectively Table 2) with grains from both types of picrites covering the full range (Fig. 12a). The range

indicates a fO_2 of approximately ΔFMQ 0 to -1.4 (Ballhaus et al., 1991), with no difference between the two types of picrite. In contrast, the V oxybarometer gives higher fO_2 and shows a difference between low- and high-Ti picrites.

Based on the V oxybarometer the fO_2 was calculated using the equation from Canil (2002)

$$\Delta NNO = \{\log[(V_{liq}/V_{chr})*24.1-1]-0.82\}/0.28$$

This equation requires the V content of the liquid (V_{liq}) and chromite (V_{chr}). As mentioned above, the whole rock compositions do not represent liquid compositions and needs to be recalculated to remove the olivine and chromite phenocrysts. The liquid compositions were estimated as described above. The chromites from low-Ti picrites have higher fO_2 than the chromites from high-Ti picrites (Fig. 12b) averaging at ΔNNO at +0.19 and ΔNNO at -0.57 respectively. These fO_2 are equivalent of ΔFMQ +0.88 and +0.12 (http://www.kaylaiacovino.com/tools-for-petrologists).

4.5 Partition Coefficients

Whereas, we accept the chromites may not have crystallized from the transporting melt, that is to say they could be antecrysts, it also is possible that they did crystallize from the transporting melt and that empirical partition coefficients can be estimated using the calculated melt compositions. Average partition coefficients are listed in Table 5 using the recalculated melt concentrations. Also shown are the partition coefficients for the samples where the smallest correction to the whole rock composition was necessary (4% olivine and 0.05% chromite removal for sample BC-04 for low-Ti picrite, and 17% olivine and 0.20 % chromite removal for sample JC-07 for the high-Ti picrite). The partition coefficients for these two samples agree with

339 the average partition coefficients indicating that calculation to estimate the melt compositions
340 has not distorted the estimated partition coefficients.

341 The partition coefficients for the 3+. 4+ and 5+ ions are generally similar to the partition
342 coefficients calculated for chromites and Cr-spinels using the experiments run between Δ
343 FMQ −2 to Δ+2 (Table 5). The 3+ site is mainly occupied by Cr and those ions with radii
344 within 15 % of the radius of Cr^{3+}, (V, Ga and Al) have partition coefficients between 1 and 4.
345 Scandium and In are also 3+ ion, but are slightly too large to substitute for Cr^{3+} and the partition
346 coefficients are therefore lower at approximately 0.2 and <0.5, respectively. The partition
347 coefficients for Ga, Al and Sc are not significantly different between chromites from high- and
348 low-Ti picrites or between chromites in the matrix and chromites in the olivine phenocrysts
349 (Table 5). In contrast the V partition coefficient for the chromites from low-Ti picrites are lower
350 than those from high-Ti picrites. We interpret this to be a result of lower fO_2 in the high-Ti
351 picrites and consequently more of the V is in the 3+ state and can more readily substitute for
352 Cr^{3+}.

353 The partition coefficients for the 4+ and 5+ ions Ti, Sn, Hf, Nb and Ta range from a high
354 of 0.8 for Ti to a low of 0.005 for Nb and Ta. The radius of Ti^{4+} is very close to that of Cr^{3+} and
355 hence despite the difference in charge the partition coefficient is only slightly below one. There
356 is a significant difference between the partition coefficient for Ti into chromites from high- and
357 low-Ti picrites, with partition coefficient being significantly lower in low-Ti picrites than high
358 Ti-picrites (0.5 vs 0.8, respectively). The Ti^{4+} substitution into the Cr^{3+} site is a coupled
359 substitution consisting of Ti^{4+} and Fe^{2+} (Minin et al., 2011). The higher partition coefficient of Ti
360 into the high-Ti picrite chromite could be because the high-Ti picrite melt was richer in FeOT
361 and thus more FeO was available. Tin and Hf have lower partition coefficients than Ti (0.2 and

0.02, respectively) probably because the differences in radii between Cr^{3+} and these elements are much larger than that of Ti. Although, Nb and Ta have similar radii to Cr^{3+} the partition coefficients are very low at approximately 0.005, reflecting the 2+ charge difference.

The empirical partition coefficients for the 2+ ions Mg, Ni, Co and Cu do not agree with the experimental determinations. Magnesium, Ni and Co partition coefficients are all slightly lower than the experimental determinations and Cu are higher. As discussed above 2+ ions may have re-equilibrated after the chromite crystallized and the lower partition coefficients could reflect this re-equilibrium. The range in partition coefficients for Cu is much wider than for the other elements and may be the result of an overestimation of the Cu content in some grains due to the boundary layer effect as discussed above.

5. Comparison with chromites from other settings.

Kamenetsky et al. (2001) proposed a plot of TiO_2 versus Al_2O_3 to distinguish chromite from lavas of different tectonic settings. We have added a field for chromite from komatiites based on the 677 samples from the GEOROC data base. The field outlined represents the contour to include 90% of the analyses. This field overlaps with the chromites from island arc tholeiites. None of the Emeishan chromites plot in the proposed LIP field. The chromites from low-Ti picrites plot towards the edge of the komatiite and MORB fields (Fig. 13). The chromites from the high-Ti picrites plot in the ocean island basalt field (Fig. 13).

In order to make a comparison using a wider range of trace elements we have plotted the chromites normalized to trace elements in our komatiite chromite (AX 37). This chromite is from the Alexo komatiite flow, which is from an Al-undepleted komatiite that has experienced only prehnite-pumpellyite metamorphism (Jolly, 1982) and thus the effects of metamorphism should

be limited. The whole rock trace element patterns from this komatiite flow show slight depletion in LREE, Nb, Ta and Th relative to HREE, indicating the magma was from a slightly depleted mantle source (Barnes, 1985). On the chromite-normalized plots the elements are plotted in order of their compatibility with crystallization of 99 % olivine and 1 % chromite, approximately cotectic proportions from a primitive magma (Roeder et al., 2006). From Ni to Zn (from right to left), the phase controlling the elements should be olivine. From Cr to Al, the phase controlling the elements should be chromite. Titanium and Sc could show the influence of pyroxene. For Sn, and Hf the elements should be controlled by the liquid composition.

The pattern of the chromites from low-Ti picrites normalized to komatiite chromite is relatively flat with most elements in the 0.3 to 3 times komatiite range (Fig. 14a). All of the samples exhibit a positive Ti anomaly at approximately twice to thrice the komatiite value and a similar enrichment in Hf. Some grains show a depletion in Sc and enrichments in Fe, Mn and Ni. The patterns for chromites from the high-Ti picrites are more variable at 0.4 to 12 times komatiite. They have larger positive Ti anomalies with Ti in the 6 to 10 times komatiite chromite and are more enriched in Hf, Sn, Ga and V at 2 to 5 times komatiite values. As is the case for the low-Ti picrites they are slightly enriched in Mn and Ni (Fig. 14b)

The World's largest PGE resource is the UG-2 chromite-rich layer from the Bushveld Complex. It is argued that the Bushveld Complex is the product of a mantle plume (Hatton 1995; Barnes and Maier, 2002, Florentini et al., 2020) and hence the magmas that formed the deposit could show similarities with LIP magmas. Therefore, we compare with the recent analyses from Langa et al. (2021) for the UG-2 of the western limb (UG-2W) of the Bushveld Complex and the chromite-rich layer of the northern limb (assumed to be similar to the UG-2) hereafter referred to as UG-2N with komatiite chromite and the chromite from the Emeishan LIP.

The UG-2W and UG-2N chromite patterns normalized to komatiite are relative flat but have large positive Ti, Ga, V and Zn anomalies at up to 6 times komatiite chromite, and are depleted in Mg (Fig. 14c and d). The enrichment of Ti, Ga, V and Zn and depletion of Mg in the UG-2 chromites indicates that the magma with which they equilibrated was more evolved than a komatiite.

The UG-2 chromite patterns show some similarities with the chromites from high-Ti picrites. In order to compare the UG-2W and UG-2N layers with the composition of the chromite from high-Ti picrite, more closely the samples have been normalized to the JC-07 chromite (the sample with highest estimation of MgO content of the high-Ti picrites; (Fig.14e and f). The UG-2W chromites are enriched in V and Zn and slightly depleted in Sc, Ti, Mg, and Ni. The UG-2N chromites have similar patterns except that V is not as enriched and they are slightly enriched in Co, Fe, Mn.

The UG-2W and UG-2N chromites are cumulate, and thus the compositions could have been modified by post-cumulate processes such as equilibration with trapped liquid. Langa et al. (2021) observed that the UG-2N chromite layer contains more interstitial silicate component than the UG-2W and argued that the UG-2N chromites have undergone equilibration with a larger trapped liquid component than the UG-2W. Thus, the higher Co, Mn, Fe and Zn observed in the UG-2N chromite could be interpreted as the product of post-cumulate reaction with a trapped liquid.

The depletion of Sc and Ti and enrichment of V, in both the UG-2W and UG-2N chromites is more difficult to explain by equilibration with trapped liquid fraction as these elements diffuse more slowly (Coulthard, al. 2021). Also, as observed in our study of the Emeishan chromites the concentrations of these elements in the inclusion chromites and matrix

chromites are similar, which we interpret to be because they diffuse more slowly. The depletion in Sc and Ti in the Bushveld chromites may reflect the effect of pyroxene crystallization as interstitial orthopyroxene is present in the case of the UG-2 chromites, thus pyroxene may have been crystallizing at the same time as chromite and competed for these elements.

Langa et al. (2021) found that $Fe^{3+}/\Sigma Fe$ is lower (0.21 to 0.23) in the chromites from the UG-2W than in chromites from UG-2N (0.23 to 0.25), which they interpret to be because the UG-2W magma was more reduced than UG-2N magma. They further argue that the northern limb rocks show evidence of *in situ* contamination by the country rocks, which could be the source of the higher oxidation. The enrichment in V in the UG-2W chromites relative to the UG-2N chromites is consistent with this argument because a more reduced magma would contain more V^{3+} which could more readily substitute into chromite. Assuming the liquid contained 200 ppm V (based on the composition of the chill zones of the Bushveld Complex, (Barnes et al., 2010) the fO_2 for the UG-2W can be estimated as approximately ΔFMQ -2 and that of UG-2N as approximately ΔFMQ -1. These estimates are somewhat lower than suggested by the $Fe^{3+}/\Sigma Fe$ found by Langa et al. (2021) of ΔFMQ -1 to 0. However, Adetunji et al. (2013) report lower $Fe^{3+}/\Sigma Fe$ from UG-2 chromites from the eastern limb of the Bushveld (0.17 to 0.2) consistent with the lower estimation of fO_2 from V. They further showed that the $Fe^{3+}/\Sigma Fe$ of the chromites was affected by subsolidus processes. Given that Fe concentrations appear to be readily affected by subsolidus diffusion and as shown above V appears to undergone less re-equilibration than Fe in the case of the Emeishan chromites we conclude that V is probably a more reliable indicator of the fO_2 than $Fe^{3+}/\Sigma Fe$.

6 Conclusions

The concentrations of 3+, 4+ and 5+ ions (Al, Ti, Sc, V, Ga, Nb, Sn, and Hf) in chromites from high- and low-Ti picrites from the Emeishan Large Igneous Province are different. The chromites from high-Ti picrites have higher concentrations of Ti, V, Nb, Sn and Hf than the chromites from low-Ti picrites. The chromites from low-Ti picrites are enriched in Al. These differences reflect the difference in the magma compositions, except for V. Whole-rock concentrations of V in both high- and low-Ti picrites are similar. The higher V content in chromites from the high-Ti picrites is attributed to a lower fO_2 in the high-Ti picrites resulting in more of the V being present as V^{3+}.

The concentrations of 2+ ions Mg, Mn, Co, Ni and Zn are similar in chromite grains from both high- and low-Ti picrites. The habit of the chromite grain influences the concentrations of 2+ ions. The chromites found in the matrix contain more Mn, Fe, and Zn than chromites included in olivine. The chromites included in olivine are richer in Mg. The concentrations of 3+, 4+ and 5+ ions are similar in both forms of chromite. Based on the difference in the behavior of the 2+ and 3+, 4+, 5+ ions we consider that the 2+ ions re-equilibrated with the olivine in the case of the inclusion chromite and the melt in the case of the matrix chromite.

Gallium, Al, V 3+ ions with radii within 15% of Cr^{3+}ions have empirical partition coefficients in the 1 to 3 range indicating that they are compatible with chromite. Scandium (also a 3+ ions) has a low partition coefficients due to its large radius. Most of the 4+ and 5+ ions (Nb, Sn, Hf, Ta) are strongly incompatible. Titanium is an exception to this with partition coefficients in the 0.5 to 0.8 range. This could be because Ti^{4+} radius is close to that of Cr^{3+}.

Relative to komatiite chromites. the Emeishan chromites are enriched in Hf, Sn, Ti, Ga, Zn and Mn. The chromites from the World's largest PGE deposit, the UG-2, show some similarities with the chromite from the Emeishan high Ti-picrites, but are more enriched in Ga,

V, Zn and Fe and depleted in Sc, Ti, Mg and Ni. These enrichments and depletions suggest that the magma with which UG-2 chromite equilibrated was more evolved than the either the komatiite or Emeishan picrites.

Declaration of Competing Interest

The authors declare that they have no known competing financial interests or personal relationships that could have appeared to influence the work reported in this paper.

Acknowledgements

The anonymous reviewers are thanked for their time and efforts to clarify this work. This study was funded by the Natural Sciences and Engineering Research Council of Canada Discovery Grant 1884-2013 (S-J B). The samples were originally collected as part of an MSc project published as Arguin et al (2016) and which was funded jointly by the Canadian Research Chair in Magmatic Metallogeny grant #950-215503 (S-JB) and State Key Laboratory of Ore Deposit Geochemistry of China: SKLODG grant #201204 to Dr. Xie-Yan Song. Dr. Song-Yue Yu is thanked for help in collection of the samples for the original study.

References

Adetunji, J., Everitt, S., Rollinson, H., 2013. New Mössbauer measurements of Fe3+/ΣFe ratios in chromites from the early Proterozoic Bushveld Complex, South Africa. Precambrian Research 228, 194-205.

Ali, J.R., Thompson, G.M., Zhou, M.-F., Song, X., 2005. Emeishan large igneous province, SW China. Lithos 79, 475-489.

Arguin, J.-P., Pagé, P., Barnes, S.-J., Yu, S.-Y., Song, X.-Y., 2016. The effect of chromite crystallization on the distribution of osmium, iridium, ruthenium and rhodium in picritic magmas: an example from the Emeishan Large Igneous Province, Southwestern China. Journal of Petrology 57, 1019-1048.

Bai M.., Hong, Z., Weiguang, Z., Zhongjie, B., Defeng, H., 2013. Platinum- Group Element Geochemical Characteristics of the Picrites and High- Ti Basalts in the Binchuan Area, Yunnan Province. Acta Geologica Sinica- English Edition 87, 158-175.

Ballhaus, C., Berry, R.F., Green, D.H., 1991. High pressure experimental calibration of the olivine-orthopyroxene-spinel oxygen geobarometer: implications for the oxidation state of the upper mantle. Contributions to Mineralogy and Petrology 107, 27-40.

Barnes, S.J., 1998. Chromite in komatiites, 1. Magmatic Controls on Crystallization and Composition. Journal of Petrology 39, 1689-1720.

Barnes, S.J., Roeder, P.L., 2001. The range of spinel compositions in terrestrial mafic and ultramafic rocks. Journal of Petrology 42, 2279-2302.

Barnes, S.-J., 1985. The petrography and geochemistry of komatiite flows from the Abitibi Greenstone Belt and a model for their formation. Lithos 18, 241-270

Barnes, S-J., Maier, W.D., 2002. Platinum-group element distributions in the Rustenburg layered suite of the Bushveld Complex, South Africa, The Geology, Geochemistry, Mineralogy and Mineral Beneficiation of Platinum-group Elements. Canadian Institute of Mining, Metallurgy and Petroleum Special Vol 57 ed L.J Cabri pp. 431-458.

Barnes, S.-J., Maier, W.D., Curl, E.A., 2010. Composition of the marginal rocks and sills of the Rustenburg Layered Suite, Bushveld Complex, South Africa: implications for the formation of the platinum-group element deposits. Economic Geology 105, 1491-1511.

Bédard, J.H., 2005. Partitioning coefficients between olivine and silicate melts. Lithos 83, 394-419.

Brenan, J.M., Finnigan, C.F., McDonough, W.F., Homolova, V., 2012. Experimental constraints on the partitioning of Ru, Rh, Ir, Pt and Pd between chromite and silicate melt: the importance of ferric iron. Chemical Geology 302, 16-32.

Canil, D., 2002. Vanadium in peridotites, mantle redox and tectonic environments: Archean to present. Earth and Planetary Science Letters 195, 75-90.

Canil, D., Fedortchouk, Y., 2001. Olivine–liquid partitioning of vanadium and other trace elements, with applications to modern and ancient picrites. The Canadian Mineralogist 39, 319-330.

Chen, L.-M., Song, X.-Y., Hu, R.-Z., Yu, S.-Y., He, H.-L., Dai, Z.-H., She, Y.-W., Xie, W., 2017. Controls on trace-element partitioning among co-crystallizing minerals: Evidence from the Panzhihua layered intrusion, SW China. American Mineralogist 102, 1006-1020.

Coulthard, D.A., Zellmer, G.F., Tomiya, A., Jégo, S., Brahm, R., 2021. Petrogenetic implications of chromite-seeded boninite crystallization experiments: Providing a basis for chromite-

melt diffusion chronometry in an oxybarometric context. Geochimica et Cosmochimica Acta 297, 179-202.

Fiorentini, M.L., O'Neill, C., Giuliani, A., Choi, E., Maas, R., Pirajno, F., Foley, S., 2020. Bushveld superplume drove Proterozoic magmatism and metallogenesis in Australia. Scientific Reports 10, 1-10.

Frost, B.R., 1991. Introduction to oxygen fugacity and its petrologic importance. Reviews in Mineralogy and Geochemistry 25, 1-9.

Garuti, G., Evgeny, E.V., Thalhammer, O.A., Zaccarini, F., 2012. Chromites of the Urals (Part 1: Overview of chromite mineral chemistry and geo-tectonic setting. Ofioliti 37, 27-53.

González-Jiménez, J.M., Griffin, W.L., Proenza, J.A., Gervilla, F., O'Reilly, S.Y., Akbulut, M., Pearson, N.J., Arai, S., 2014. Chromitites in ophiolites: How, where, when, why? Part II. The crystallization of chromitites. Lithos 189, 140-158.

Hanski, E., Kamenetsky, V.S., Luo, Z.-Y., Xu, Y.-G., Kuzmin, D.V., 2010. Primitive magmas in the Emeishan Large Igneous Province, southwestern China and northern Vietnam. Lithos 119, 75-90.

Hatton, C.J., 1995. Mantle plume origin for the Bushveld and Ventersdorp magmatic provinces. Journal of African Earth Sciences 21, 571-577.

Horn, I., Jenner, G., 1994. Compositional dependencies of the partition coefficients for Zr, Nb, Ta, Hf and selected transition elements between spinel and melt. Geochim. Cosmochim. Acta 51, 1071-1081.

Irvine, T., 1975. Crystallization sequences in the Muskox Intrusion and other layered complexes-origin of chromitite layers and similar deposits of other magmatic ores. Geochimica et Cosmochimica Acta 39, 921-1020.

562 Jenkins, M.C., Mungall, J.E., 2018. Genesis of the peridotite zone, Stillwater Complex, Montana,
563 USA. Journal of Petrology 59, 2157-2189.
564 Jolly, W.T., 1982. Progressive metamorphism of komatiites and related Archean laas of the
565 Abitibi area, Canada. In: Komatiites (N. T. Arndt & E. G. Nisbet, eds.). Geoge Allen and
566 Unwin, London, U.K.
567 Kamenetsky, V.S., Crawford, A.J., Meffre, S., 2001. Factors controlling chemistry of magmatic
568 spinel: an empirical study of associated olivine, Cr-spinel and melt inclusions from
569 primitive rocks. Journal of Petrology 42, 655-671.
570 Kamenetsky, V.S., Chung, S.-L., Kamenetsky, M.B., Kuzmin, D.V., 2012. Picrites from the
571 Emeishan Large Igneous Province, SW China: a compositional continuum in primitive
572 magmas and their respective mantle sources. Journal of Petrology 53, 2095-2113.
573 Langa, M.M., Jugo, P.J., Leybourne, M.I., Grobler, D.F., Adetunji, J., Skogby, H., 2021.
574 Chromite chemistry of a massive chromitite seam in the northern limb of the Bushveld
575 Igneous Complex, South Africa: correlation with the UG-2 in the eastern and western
576 limbs and evidence of variable assimilation of footwall rocks. Mineralium Deposita 56,
577 31-44.
578 Latyshev, A., Rad'ko, V., Veselovskiy, R., Fetisova, A., Pavlov, V., 2020. Correlation of the
579 Permian-Triassic ore-bearing intrusions of the Norilsk region with the volcanic sequence
580 of the Siberian Traps based on the paleomagnetic data. Economic Geology 115, 1173-
581 1193.
582 Li, C., Tao, Y., Qi, L., Ripley, E.M., 2012. Controls on PGE fractionation in the Emeishan
583 picrites and basalts: constraints from integrated lithophile–siderophile elements and Sr–
584 Nd isotopes. Geochimica et Cosmochimica Acta 90, 12-32.

585 Li, J., Wang, X.-C., Ren, Z.-Y., Xu, J.-F., He, B., Xu, Y.-G., 2014. Chemical heterogeneity of
586 the Emeishan mantle plume: evidence from highly siderophile element abundances in
587 picrites. Journal of Asian Earth Sciences 79, 191-205.
588 Longerich, H.P., Jackson, S.E., Günther, D., 1996. Inter-laboratory note. Laser ablation
589 inductively coupled plasma mass spectrometric transient signal data acquisition and
590 analyte concentration calculation. Journal of Analytical Atomic Spectrometry 11, 899-
591 904.
592 Locmelis, M., Pearson, N.J., Barnes, S.J., Fiorentini, M.L., 2011. Ruthenium in komatiitic
593 chromite. Geochimica Cosmochimica Acta 75, 3645-3661.
594 Maier, W.D., Barnes, S.-J., Karykowski, B., 2016. A chilled margin of komatiite and Mg-rich
595 basaltic andesite in the western Bushveld Complex, South Africa. Contributions to
596 Mineralogy and Petrology 171, 57.
597 Minin, V., Prugov, V., Podgornykh, N., Kovyazin, S., Kholodova, L., 2011. Composition of
598 chromites from kimberlites of the Botuobinskaya pipe in Yakutia. Geology of Ore
599 Deposits 53, 626-638.
600 Naldrett, A.J., Wilson, A., Kinnaird, J., Yudovskaya, M., Chunnett, G., 2012. The origin of
601 chromitites and related PGE mineralization in the Bushveld Complex: new mineralogical
602 and petrological constraints. MIneralium Deposita 47, 209-232.
603 Nicklas, R.W., Puchtel, I.S., Ash, R.D., 2016. High-precision determination of the oxidation
604 state of komatiite lavas using vanadium liquid-mineral partitioning. Chemical Geology
605 433, 36-45.
606 Nikolaev, G. S., Ariskin, A. A., Barmina, G. S., 2018. SPINMELT-2.0: Simulation of spinel–
607 melt equilibrium in basaltic systems under pressures up to 15 kbar: II. Description of the

program package, the topology of the Cr-spinel–melt model system, and petrological implications. Geochemistry International 56, 125–135.

Nixon, G.T., Cabri, L.J., Laflamme, G.J.H., 1990. Platinum-group element mineralization in lobe and placer deposits associated with the Tulameen Alaskan-type Complex, British Columbia. Canadian Mineralogist 28, 503-535.

Pagé, P., Barnes, S.-J., 2009. Using trace elements in chromites to constrain the origin of podiform chromitites in the Thetford Mines ophiolite, Québec, Canada. Economic Geology 104, 997-1018.

Paton, C., Hellstrom, J., Paul, B., Woodhead, J., Hergt, J., 2011. Iolite: Freeware for the visualisation and processing of mass spectrometric data. Journal of Analytical Atomic Apectrometry 26, 2508-2518. 26, 2508-2518.

Righter, K., Campbell, A.J., Humayun, M., Hervig, R.L., 2004. Partitioning of Ru, Rh, Pd, Re, Ir and Au between Cr-bearing spinel, olivine, pyroxene and silicate melts. Geochimica and Cosmochimica Acta 68, 867-880

Roeder, P.L., Emslie, R.F., 1970. Olivine-liquid equilibrium. Contributions to Mineralogy and Petrology 29, 275-289.

Roeder, P.L., Campbell, I.H., 1985. The effect of postcumulus reactions on composition of chrome-spinels from the Jimberlana intrusion. Journal of Petrology 26, 763-786.

Roeder, P., Gofton, E., Thornber, C., 2006. Cotectic proportions of olivine and spinel in olivine-tholeiitic basalt and evaluation of pre-eruptive processes. Journal of Petrology 47, 883-900.

Scowen, P., Roeder, P., Helz, R.T., 1991. Reequilibration of chromite within Kilauea Iki lava lake, Hawaii. Contributions to Mineralogy and Petrology 107, 8-20.

631 Shellnutt, J.G., 2014. The Emeishan large igneous province: A synthesis. Geoscience Frontiers 5,
632 369-394.
633 Solovova, I., Yudovskaya, M., Kinnaird, J., Wilson, A., Zinovieva, N., 2021. A siliceous
634 komatiitic source of Bushveld magmas revealed by primary melt inclusions in olivine.
635 Lithos 388, 106094.
636 Song, X.-Y., Zhou, M.-F., Hou, Z.-Q., Cao, Z.-M., Wang, Y.-l., Li, Y., 2001. Geochemical
637 Constraints on the Mantle Source of the Upper Permian Emeishan Continental Flood
638 Basalts, Southwestern, China. International Geology Review 43, 213-225.
639 Song, X.-Y., Zhou, M.-F., Cao, Z.-M., Sun, M. Wang, Y.-L., 2003. Ni-Cu-(PGE) magmatic
640 sulfide deposits in the Yangliuping area, Permian Emeishan igneous province, SW China.
641 Mineralium Deposita 38, 831-843.
642 Song, X.-Y., Zhou, M.-F., Cao, Z.-M., 2004. Genetic relationships between base-metal sulfides
643 and platinum-group minerals in the Yangliuping Ni-Cu-(PGE) sulfide deposit,
644 southwestern China. The Canadian Mineralogist 42, 469-483.
645 Song, X.-Y., Zhou, M.-F., Keays, R. R., Cao, Z.-M., Sun, M., Qi, L., 2006. Geochemistry of the
646 Emeishan flood basalts at Yangliuping, Sichuan, SW China: implications for sulfide
647 segregation. Contributions to Mineralogy and Petrology 152, 53-74.
648 Tao, Y., Li, C., Hu, R., Ripley, E. M., Du, A., Zhong, H., 2007. Petrogenesis of the Pt-Pd
649 mineralized Jinbaoshan ultramafic intrusion in the Permian Emeishan Large Igneous
650 Province, SW China. Contributions to Mineralogy and Petrology 153, 321-337.
651 Tao, Y., Li, C., Song, X.-Y., Ripley, E. M., 2008. Mineralogical, petrological, and geochemical
652 studies of the Limahe mafic-ultramafic intrusion and associated Ni-Cu sulfide ores, SW
653 China. Mineralium Deposita 43, 849-872.

654 Tao, Y., Li, C., Hu, R., Qi, L., Qu, W., Du, A., 2010. Re-Os isotopic constraints on the genesis of
655 the Limahe Ni-Cu deposit in the Emeishan large igneous province, SW China. Lithos
656 119, 137-146.
657 Tolstykh, N., Shvedov, G., Polonyankin, A., Korolyuk, V., 2020. Geochemical Features and
658 Mineral Associations of Differentiated Rocks of the Norilsk 1 Intrusion. Minerals 10,
659 688.
660 Wang, C. Y., Zhou, M.-F., 2011. Chalcophile element geochemistry and petrogenesis of high-Ti
661 and low-Ti magmas in the Permian Emeishan Large I,gneous province, SW China.
662 Contributions to Mineralogy and Petrology 161, 237-254.
663 Wang, C.Y., Zhou, M.-F., Zhao, D., 2005. Mineral chemistry of chromite from the Permian
664 Jinbaoshan Pt–Pd–sulphide-bearing ultramafic intrusion in SW China with petrogenetic
665 implications. Lithos 83, 47-66.
666 Wang, C. Y., Zhou, M.-F., Keays, R. R., 2006. Geochemical constraints on the origin of the
667 Permian Baimazhai mafic-ultramafic intrusion, SW China. Contributions to Mineralogy
668 and Petrology 152, 309-321.
669 Wang, C. Y., Zhou, M.-F., Qi, L., 2007. Permian flood basalts and mafic intrusions in the
670 Jinping (SW China)-Song Da (northern Vietnam) district: Mantle sources, crustal
671 contamination and sulfide segregation. Chemical Geology 243, 317-343.
672 Wang, C.Y., Zhou, M.-F., Zhao, D., 2008. Fe–Ti–Cr oxides from the Permian Xinjie mafic–
673 ultramafic layered intrusion in the Emeishan large igneous province, SW China:
674 crystallization from Fe-and Ti-rich basaltic magmas. Lithos 102, 198-217.

675 Wijbrans, C.H., Klemme, S., Berndt, J., Vollmer, C., 2015. Experimental determination of trace
676 element partition coefficients between spinel and silicate melt: the influence of chemical
677 composition and oxygen fugacity. Contributions to Mineralogy and Petrology 169, 45.
678 Wilson, A.H., 2012. A chill sequence to the Bushveld Complex: insight into the first stage of
679 emplacement and implications for the parental magmas. Journal of Petrology 53, 1123-
680 1168.
681 Xiao, L., Xu, Y. G., Mei, H. J., Zheng, Y. F., He, B., Pirajno, F., 2004. Distinct mantle sources
682 of low-Ti and high-Ti basalts from the western Emeishan large igneous province, SW
683 China: implications for plume-lithosphere interaction. Earth and Planetary Science
684 Letters 228, 525-546.,
685 Xu, Y., Chung, S.-L., Jahn, B.-M., Wu, G., 2001. Petrologic and geochemical constraints on the
686 petrogenesis of Permian-Triassic Emeishan flood basalts in southwestern China. Lithos
687 58, 145-168.
688 Zhang, Z. C., Mao, J., Mahoney, J. J., Wang, F., Qu, W., 2005. Platinum group elements in the
689 Emeishan large igneous province, SW China: Implications for mantle sources.
690 Geochemical Journal 39, 371-382.
691 Zhang, Z. C., Mahoney, J. J., Mao, J. W., Wang, F. S., 2006. Geochemistry of picritic and
692 associated basalt flows of the Western Emeishan flood basalt province. Journal of
693 Petrology 47, 1997-2019.
694 Zhong, H., Zhu, W. G., 2006. Geochronology of layered mafic intrusions from the Pan-Xi area
695 in the Emeishan large igneous province, SW China. Mineralium Deposita 41, 599-606.
696 Zhou, M.-F., Robinson, P. T., Lesher, C. M., Keays, R. R., Zhang, C. J., Malpas, J., 2005.
697 Geochemistry, petrogenesis, and metallogenesis of the Panzhihua gabbroic layered

intrusion and associated Fe-Ti-V-oxide deposits, Sichuan Province, SW China. Journal of Petrology 46, 2253-2280.

Zhou, M.-F., Arndt, N. T., Malpas, J., Wang, C. Y., Kennedy, A. K., 2008. Two magma series and associated ore deposit types in the Permian Emeishan large igneous province. Lithos 103, 352-368.

Zhou, M.-F., Chen, W. T., Wang, C. Y., Prevec, S. A., Liu, P. P., Howarth, G. H., 2013. Two stages of immiscible liquid separation in the formation of Panzhihua-type Fe-Ti-V oxide deposits, SW China. Geoscience Frontiers 4, 481-502.

Figure Captions

Fig. 1. Schematic geological map showing locations of sample localities for this study and the distribution of flood basalt successions in the Emeishan Province, southwestern China LMS Longmenshan thrust fault. Modified after Kamenetsky et al. (2012).

Fig. 2 Photomicrograph and element maps showing variations in element concentrations of a chromite inclusion in olivine. Chr = chromite. Note that with the exception of Cu the elements show the similar concentrations across the grain.

Fig. 3 Photomicrograph and variations in element concentrations of a chromite in the matrix. Chr=chromite, Ti-Mgt = Ti-rich magnetite, Note: a) that there is an overgrowth of Ti-rich magnetite on the chromite grain; b) with the exception of Cu the elements show the similar concentrations across the chromite grain.

Fig. 4. Whole rock concentrations of MgO vs: a) Ni, b) Co, c) MnO, d) Zn, e) FeOt, f) Cr_2O_3. FeOT = all Fe as FeO. Note those elements compatible with olivine Ni and Co show a positive correlation with MgO. Those elements with partition coefficients of approximately 1 into olivine MnO, Zn and FeOt show a flat trend. The positive correlation of MgO and Cr_2O_3 implies that in addition to olivine chromite was crystallizing.

Fig. 5 Whole rock concentrations of MgO vs a) TiO_2, b) Al_2O_3, c) Sn, d) Hf and e) Nb. All of these elements show a negative correlation with MgO consistent with olivine crystallization. The high-Ti picrites are enriched in TiO_2, Sn and Hf relative to the low-Ti picrites and poorer in Al_2O_3. The high-Ti picrites and the low-Ti Binchuan picrites are enriched in Nb relative to the Dali picrites. Literature data from Bai et al. (2014), Li et al. (2012), Li et al. (2014), Zang (2005).

Fig. 6 Whole rock concentrations of MgO vs a) V, b) Cu, c) Ga and d) Sc. Vanadium, Cu and Ga show a negative correlation with MgO for the picrites consistent with olivine crystallization, however there does not appear to be a difference in concentrations between the high-Ti and low-Ti picrites. Scandium shows no clear trends. Literature data from Bai et al. (2014), Li et al. (2012), Li et al. (2014), Zang (2005).

Fig. 7 TiO_2 vs; a) Al_2O_3; b) Cr_2O_3 c) MgO and d) FeOt concentrations in chromites. Stars show the composition of the chromite as calculated by SPINMELTS2 for the melt composition of highest and lowest MgO contents. These compositions cover the observed range of compositions for TiO_2, versus Al_2O_3 and Cr_2O_3, however the calculated chromite compositions are contain much less FeOt and much more MgO than the observed compositions.

Fig. 8 Comparison of a) FeOT, b) MnO, c) Co, d) Zn concentrations in inclusions and matrix chromites showing that matrix chromites are enriched in FeOT, MnO and Zn.

Fig. 9 Comparison of a) Al2O3, b) TiO2, c) Sc, d) V, e) Ga and f) Hf concentrations in inclusions and matrix chromites showing that concentrations of these elements are similar in and inclusion chromites.

Fig. 10 Plots of whole rock concentrations versus chromite element concentrations illustrating that the chromite composition reflect the differences in whole rock compositions with chromites from high-Ti picrites being enriched in; a) TiO_2, b) Nb, c) Sn, d) Hf and e)Ta. In contrast V concentrations in whole rock from both high and low-Ti picrites are similar but the chromites from high-Ti picrites are enriched in V relative to the chromites from low-Ti picrites f).

748 Fig. 11 Plots of whole rock TiO_2 vs chromite concentrations of a) Mn, b) Co, c) Ni, d) Zn, e) Sc
749 and f) Ga showing that the concentrations of these elements in chromite from high-Ti and low-Ti
750 picrites are similar.

751 Fig. 12 a) $Fe^{3+}/\Sigma Fe$ vs TiO_2 in chromite; b) calculated fO_2 based on V content expressed as
752 ΔNNO versus TiO_2 concentrations in whole rock. Note that $Fe^{3+}/\Sigma Fe$ covers the same range in
753 all chromites indicating no difference fO_2 among chromites, whereas fO_2 calculated based on V
754 content shows that the chromites from high-Ti picrites have a lower *f*O2 than the chromites from
755 low-Ti picrites. *f*O2.

756 Fig. 13 Plot of Al_2O_3 versus TiO_2 contents of chromite to compare with the fields of chromite
757 compositions from the literature as defined by Kamenetsky et al. (2001) with the addition of a
758 field for komatiites (this work) based on GEOROC. The chromites from low-Ti picrites overlap
759 with the komatiite (kom) and arc-tholeiite fields. The chromite from high-Ti picrites overlap
760 with ocean island basalt (OIB) field. Neither plot in the large igneous province (LIP) field.

761 Fig. 14 a) to d) Composition of the Emeishan and UG-2 chromites normalized to komatiite
762 chromite with elements plotted in order of compatibility with crystallization of 99 % olivine and
763 1% chromite. a) Low-Ti picrites, b) High-Ti picrites, c) UG-2 Western limb Bushveld, d) UG-2
764 northern limb Bushveld. e) and f) Composition of UG-2 chromites normalized to chromite from
765 high-Ti picrites. UG-2 data from Langa et al. (2021).

766

Differences in composition of chromites from low-Ti and high-Ti picrites of the Emeishan Large Igneous Province and comparison with chromites of the UG-2 platinum-deposit of the Bushveld Complex.

Sarah-Jane Barnes*[1], Eduardo T Mansur[1,2], Philippe Pagé [1,3]

[1]Sciences de la Terre, Université du Québec à Chicoutimi, 555 boulevard de l'université, Québec G7H 2B1, Canada

[2]Geological Survey of Norway, P.O. Box 6315 Torgarden, NO-7491 Trondheim

[3] IOS Services Géoscientifiques Inc, 1319 Saint-Paul boul., Chicoutimi G7J 3Y2, Canada

*Corresponding Author

e-mail: sjbarnes@uqac.ca

Keywords: Chromite, trace elements, Emeishan, picrite, UG-2, Platinum-group element ore deposits.

ABSTRACT

Chromite is among the first minerals to crystallize from mantle derived magmas and one of the last to be consumed during partial melting of the mantle. Chromite is also an important mineral in major ore deposits of Cr and Pt. The composition of chromite could, therefore be of use in interpreting the petrogenetic conditions during partial melting of the mantle, crystallization of primitive magmas and formation of Pt and Cr ore deposits. However, most mafic rocks contain very little chromite and post-crystallization processes such as re-equilibration during cooling, metamorphism and weathering could change the composition. The composition of chromites from high- and low-Ti picrites from the Emeishan large igneous province have been determined to assess the degree to which the chromite compositions reflect the melt compositions. Aluminium, Sc, Ti, Ga, Nb, Sn, Hf and Ta concentrations in the chromites do appear to reflect the melt compositions in that they correlate with the whole rock compositions and have empirical partition coefficients similar to those determined in experiments. The V contents of both types of picrite are similar, but concentrations of chromites from high-Ti picrites are higher than those of low-Ti picrites. This can be explained if, in the high-Ti picrite more of the V was in the V3+ state (which can more readily substitute into chromite than V4+ or V5+) than in the low-Ti picrite. This implies that fO_2 was lower for high-Ti picrites than low-Ti picrites. Concentrations of elements with a 2+ charge, Mg, Mn, Fe, Co, Ni and Zn are different in chromites included in olivine and chromites in the matrix and appear to have re-equilbrated. The compositions of the UG-2 chromites from the World's largest Pt deposit show some similarities with the chromites from the high-Ti picrite, but are depleted in Sc and Ti and enriched in Ga and Al.

Formatted: Tab stops: 3.25", Centered

1. Introduction

The advent of laser ablation inductively coupled plasma-mass spectrometry (LA-ICP-MS) analyses has opened the opportunity to document trace element concentrations in minerals down to ppm or even ppb level. These observations have been used in petrogenetic studies and for mineral exploration. Chromite is of particular interest. In the case of petrogenetic studies, it of interest because it appears early in the crystallization of mantle derived magmas and is one of the last minerals to be consumed during partial melting of the mantle. Consequently, there are numerous recent studies of trace elements in chromites from rocks representing mantle fragments, ophiolites and nodules, with aim of establishing the type of magma that the chromite crystallized from (Pagé and Barnes, 2009; Gonzalez-Jimenez et al., 2014; Zhou et al., 2014. Chromite from komatiite has also been studied to document the oxygen fugacity of the early earth (Canil, 2002; Nicklas et al., 2016. In addition, Kamenetsky et al. (2001) proposed a plot of TiO_2 vs Al_2O_3 to distinguish chromites from volcanic rocks of various tectonic settings.

The trace element content of chromites is also of interest in exploration for ore deposits. For example, the concentration of Ru in chromite has been proposed as an exploration technique (Locmellis et al., 2011). The largest platinum-group element (PGE) deposit in the world, the UG-2, of the Bushveld Complex consists of massive chromitite layers (Naldrett et al., 2012). Platinum deposits are also found in association with chromitites from zoned complexes of the Urals (Garuti et al., 2012) and British Columbia (Nixon et al., 1990). Possibly the trace element content of the chromites from different settings are different and could be used in exploration programs. On the petrogenetic side it might be possible to deduce the composition of the magmas from which chromite crystallized and thus help in understanding how the ores form. However, before this can be accomplished, it is necessary to establish to whether trace element contents of chromite record the composition of the melt from which they crystallized.

Many of the large Ni-Cu-PGE deposits (Bushveld and Stillwater Complexes, the Great Dyke and Noril'sk-Talnakh) are thought to have formed either from komatiite magmas or picrites contaminated with continental crust material (Barnes et al., 2010; Wilson et al., 2012; Maier et al., 2016; Jenkins and Mungall, 2018; Latyshev et al., 2020; Tolstykh et al., 2020; Solovova et al., 2021). In the current study we assess whether chromite compositions are representative of the magma compositions by examining the compositions of chromite grains from both high- and low-Ti picrites from the Emeishan Large Igneous Province (LIP) of China. The low-Ti and high-Ti picrite melts have different Al, Ti, Fe, Nb, Sn, Hf and Ta concentrations. We show that this difference is reflected in the chromite compositions except for Fe. We also show that the composition of the chromite grains is influenced by their habit. Chromite grains occur in two main habits - enclosed in olivine phenocrysts (hereafter referred to as inclusion chromites) and in the fine-grained matrixes (hereafter referred to as matrix chromites). The concentrations of Al, Sc, Ti, V, Ga, Nb, Sn, Hf and Ta are the similar for both types of grain. Whereas inclusion chromite are richer in MgO and Co and poorer in FeO, MnO and Zn than matrix chromites. We also show that the trace elements in chromites from the high Ti-picrites show some similarities with the trace elements content of the UG-2 chromites.

2. Geological Setting.

The Emeishan LIP province occurs in south-western China covering an area of > 250,000 km^2 in the Yunnan, Sichuan and Guizhou Provinces, for a total volume of 0.3 x 10^6 km^3 (Ali et al., 2005~~.~~). The lavas were emplaced over a short period 1–2 Ma; Ali et al., 2005) at around 260 Ma. The lava sequence ranges in thickness from 1000 to more than 5000 m in the western part of the province, and from 200 to 2600 m in the eastern part (Shellnutt, 2014) and consists mostly of tholeiitic basalts which represent more than 95% of the magma volume (Xiao et al., 2004;

Hanski et al., 2010). Picrites are mainly found in the western part of the province (Song et al., 2001; Xu et al., 2001; Xiao et al., 2004; Zhang et al., 2005, 2006; Hanski et al., 2010) and in the Jinping area in southern Yunnan Province close to the China–Vietnam border (Wang et al., 2007). The Emeishan picritic flows are mainly observed in the lower and middle parts of the volcanic sequences and can reach several tens of metres in thickness (Xu et al., 2001; Xiao et al., 2004; Zhang et al., 2005, 2006, 2008).

In addition to the volcanic rocks, the Emeishan LIP also contains intrusive rocks including numerous mafic to ultramafic dikes and intrusions which are mainly exposed in the Panxi region due to several N–S-trending faults (Zhou et al., 2008. Two main types of mineral deposits are present: 1) Ni–Cu–(PGE) sulfide deposits; and 2) Fe–Ti–V oxide deposits. The magmatic sulfide deposits are found mainly in small, primitive intrusions throughout the entire flood basalt province. They include Ni–Cu–(PGE) sulfide deposits hosted by mafic–ultramafic intrusions (Song et al., 2003, 2004, 2006; Wang and Zhou, 2011~~06~~; Wang et al., 2006; Tao et al., ~~2008,~~ 2010) and PGE mineralization within ultramafic rocks (Jinbaoshan: Wang et al., 2005, 2008; Tao et al., 2007). In contrast, the Fe–Ti–V oxide deposits occur in larger and more evolved intrusions which are mainly distributed in the Panxi region along major N–S-trending faults (e.g. Taihe, Xinjie, Baima, Hongge and Panzhihua: Zhou et al., 2005, 2008, 2013; Zhong and Zhu, 2006, Chen et al., 2017).

Based mainly on their Ti/Y ratios, Xu et al. (2001) classified the tholeiitic basalts into low-Ti basalts which have Ti/Y < 500, and high-Ti basalts with Ti/Y > 500. Zhou et al. (2013) proposed that the mafic–ultramafic intrusions that host the Fe–Ti–V oxide deposits were formed from high-Ti basalts, whereas the Ni–Cu sulfide-bearing intrusions are genetically associated with the low-Ti magma series.

3. Materials and Methods

The samples used in this study were previously studied by Arguin et al. (2016) who investigated the role chromite plays in controlling PGE. The samples are fresh to slightly weathered picrites and were collected mainly from road cuts in four locations: Dali, Binchuan, Jianchuan and Lijiang, in the western part of the Emeishan LIP (Fig. 1). The Lijiang area includes the Shiman and Daju lavas. In addition, three samples from a subvolcanic sill from the Ertan area, close to Panzhihua (Sichuan Province), were also included. The UTM co-ordinates for each sample are provided in Electronic Supplementary Material (ESM1 Table 1). In general, the outcrops where samples were collected are moderately to highly weathered due to a subtropical monsoon climate. Care was taken to collect samples from the preserved parts of the outcrops.

Samples were crushed in a steel jaw crusher and then pulverized in Al-ceramic shatter box at LabMaTer, Université du Québec à Chicoutimi (UQAC). The whole rocks were analyzed for major oxides, by X-ray fluorescence, and for trace elements, ICP-MS on solutions obtained, after the powders had been dissolved by four acids in a closed vessel, at Geoscience Laboratories, Sudbury. Reference materials (ESM 1 Table 2) were analyzed in the same batch and the results agree with working values. Individual whole-rock compositions recalculated to 100% anhydrous are listed in (ESM 1 Table 3) and averages are shown in Table 1.

Polished thin sections (30 μm thick) were made of each sample. These were examined with a petrographic microscope and chromite grains were selected for *in situ* analysis. The major elements were determined on a CAMECA SX100 microprobe with wavelength dispersive spectrometry at the Université Laval, Québec City. These results have been previously reported by Arguin et al. (2016). The average analyses are reported in Table 2.

The concentration of major minor and trace elements in chromite were determined by LA-ICP-MS at LabMaTer using an Excimer 193 nm RESOlution M-50 laser ablation system (Australian Scientific Instrument) equipped with a double volume cell S-155 (Laurin Technic) and coupled with an Agilent 7900 mass spectrometer. The LA-ICP-MS tuning parameters were a laser frequency of 10 Hz, a power of 3 mJ/pulse, a dwell time of 7.5 ms, a rastering speed of 5 to 10 μm/s, and a fluence of 5 J/cm^2. Line scans across the surface of grains were made with beam sizes of 55 or 44 μm, depending on grain size. The gas blank was measured for 30s before switching on the laser for around 60s. The ablated material was carried into the ICP-MS by an Ar–He gas mix at a rate of 0.8–1 L/min for Ar and 350 mL/min for He, and 2mL/min of nitrogen was also added to the mixture. Data reduction was carried out using the Iolite package for Igor Pro software (Paton et al., 2011). Maps of the element distribution were made of some chromite grains using the same parameters with various stage movement speeds to optimize spatial resolution and analysis time of the areas being mapped. The maps were generated using the Iolite package based on the time-resolved composition of each element. The maps indicate the relative concentration of the elements and are semi-quantitative.

The isotopes ^{29}Si, ^{44}Ca, ^{31}P, ^{33}S, ^{75}As, ^{121}Sb, ^{209}Bi, were monitored in order to exclude inclusions of; silicate, carbonate, apatite and sulfide minerals. Inclusions were rare and excluded from the analyses. The isotopes ^{24}Mg, ^{27}Al, ^{45} Sc, ^{49}Ti, ^{51}V, ^{52}Cr, ^{55}Mn, ^{57}Fe, ^{59}Co, ^{60}Ni, ^{63}Cu, ^{66}Zn, ^{71}Ga, ^{89}Y, ^{93}Nb, ^{95}Mo ^{101}Ru, ^{103}Rh, ^{108}Pd, ^{111}Cd, ^{115}In, ^{118}Sn, ^{178}Hf, ^{181}Ta, ^{185}Re, ^{189}Os, ^{193}Ir, ^{195}Pt, ^{197}Au were used to determine the concentrations of these elements. The possibility of interference of ^{53}Cr^{40}Ar on ^{93}Nb was investigated. However, there appears to be no correlation between Cr and Nb, for example Nb concentrations in the in house reference chromites AX37 and MIA which contain 55 and 60 weight percent respectively Cr_2O_3 are 0.015 ppm (close to

detection limit). Hence the Cr interference on Nb was considered negligible. The concentrations of Sn are too low for ^{115}Sn to produce a significant interference on ^{115}In, and were ignored.

External calibration was carried out using three reference materials. GSE-1g with a composition close to a basaltic glass and doped with ~400 ppm of most trace elements supplied by USGS was used for minor and trace elements, except the PGE, Au and S. Laflamme Po727 a FeS dopped with ~ 40 ppm of each PGE and Au was used for the PGE and Au. A natural chromite, M1A (mantle chromite from the Thetford ophiolite) was used for the major elements Al, Mg and Cr. ^{57}Fe was used for internal calibration. Natural chromites from two in-house reference materials AX 37 (a komatiite) and M1A (ophiolite), and GProbe 6, a basaltic glass were used as monitors. The results obtained for the monitors agree within analytical error with the working values (ESM 1, Table 4). Averages obtained for the Emeishan chromites by LA-ICP-MS are reported in Table 3 a full list is available in (ESM 1, Table 5).

4. Results and Interpretation

4.1 Petrography

The picrites have a porphyritic texture and contain 10 to 45% (modal) phenocrysts of olivine (0.2 to 10 mm) in a fine grained (<0.1 mm) matrix of clinopyroxene, plagioclase, oxide and devitrified glass (Fig 2a of Arguin et al., 2016). Chromite (0.05 to 0.8 mm) is present in a small amounts (<1% modal) in three habits: a) as inclusions in the olivine phenocrysts, (Fig. 2a); b) as isolated grains in the matrix (Fig. 3a), and c) at the contact between the olivine phenocrysts (Fig. 2b of Arguin et al., 2016.

The olivine is euhedral to sub-euhedral with a narrow (<0.1 mm) rim with difference in birefringence colors indicating a sharp compositional change. Microprobe analyses show that the olivine phenocrysts compositions range from Fo_{84} to Fo_{88} in the high-Ti picrites and Fo_{86} to Fo_{92}

in the low Ti-picrites (Arguin et al., 2016) similar to the range previously reported from the Emeishan picrites (Kamenetsky et al., 2012). The rims show sharply lower Fo contents (Arguin et al., 2016). Some of the olivine grains have been variably serpentinized.

The inclusion chromites are euhedral with sharp boundaries with olivine (Fig. 2). Maps of the major and trace element distribution made by LA-ICP-MS show that the grains and are compositionally unzoned (Fig. 2), except for Cu. There is appears to be, a narrow rim of Cu enrichment at the margins of the grains (<10 μm). The chromites in the matrix are also euhedral but have narrow (<0.05 mm) titano-magnetite overgrowths (Fig. 3). The matrix chromites are unzoned, except as in the case of the inclusion chromites, there is a narrow rim enriched in Cu. The titano-magnetite rims are enriched in Ti, V, Mn, Fe, Ni, Zn, Nb, Sn and Hf, these rims were excluded from the chromite analyses.

4.2 Whole rock Composition.

Due to the presence of the olivine and chromite phenocrysts the whole rock compositions of the picrites do not represent the composition of the melt. The whole rock compositions represent a mixture of olivine + chromite and transporting melt. Based on melt inclusions in olivine Hanski et al. (2010) and Kamenetsky et al. (2012) estimated highest the MgO content of parental liquids in the Emeishan picrites to be approximately 18 weight percent MgO for the high-Ti picrites and 21 weight percent for the low-Ti picrites. Based on the highest Fo contents of the olivine, Hanski et al. (2010) estimated the highest MgO contents of the parental liquids to be from 20 to 23 weight percent. Based on the highest Fo contents of the olivine observed in our sample set, Arguin et al. (2016) estimated the MgO content of the most primitive parental liquids to be 21 weight percent for low Ti picrites, and 18 weight percent for the high-Ti picrite.

For the purposes of characterizing the chromites, our work will concentrate only on the whole-rock distribution of the elements that can be determined in chromite. Nickel and Co show positive correlations with MgO, whereas FeO_T (all Fe expressed as FeO), MnO and Zn concentrations do not change with MgO content (Fig. 4a to e). These observations are consistent with the partition coefficients for Ni and Co into olivine being higher than 1 and those of Mn and Zn being close to one (Bédard,~~Bedard~~, 2005). The low-Ti and high-Ti picrites plot along the same lines, except for FeO_T. The high-Ti picrites are richer in FeO_T at a given MgO than the low-Ti picrites.

Chrome also shows a positive correlation with MgO, which is not due to olivine control because; a) the concentration of Cr in olivine (<600 ppm, Arguin et al., 2016) is much lower than that observed in the rocks, and b) the partition coefficient of Cr into olivine for magmas with 12-20 wt % MgO is less than 1 (~0.5 to 0.6, Bédard,~~Bedard~~, 2005). Both observations indicate that in addition to olivine, chromite has accumulated in the rocks. The regression line through the picrite samples is Cr = 93.5*MgO-13.8. At 47 weight percent MgO (average MgO content of our olivines) there would be 4380 ppm Cr present. The average Cr content of olivine is 550 ppm thus 3850 ppm Cr is in excess. The Cr content of our chromite is on average 322980 ppm. Dividing the excess Cr by Cr content of chromite gives 1.2 weight percent chromite present along with 98.8 percent olivine, which seems reasonable as it is close to cotectic portions (Roeder et al., 2006).

Elements incompatible with olivine; Ti, Al, Sn, Hf, Nb, Ta, V, Cu, Ga (Bédard, ~~Bedard,~~ 2005) all show negative correlations with MgO (Fig. 5a to f and 6a to c) consistent with olivine fractionation and/or accumulation. These elements may also be divided into those showing differences between the high-Ti picrites and low-Ti picrites; Ti, Al, Sn, Hf, Nb, Ta (Fig. 5a to f,

Formatted: Font: (Default) Times New Roman, 12 pt

Table 2, and those present at similar levels in both types of picrites Ga, V and Cu (Fig. 6a to c, Table 2). Titanium, Sn and Hf are present at higher levels and Al at lower levels in high-Ti picrites than in low-Ti picrites (Fig. 5a to d). Niobium and Ta do not behave consistently; the Dali picrites contain less Nb and Ta than the high-Ti picrites, whereas the Binchuan contain similar levels to the high-Ti picrites (Fig. 5e and f). For both types of the picrites Sc does not appear to vary with MgO content and is present at 20 to 30 ppm, although in the basalts it starts to fall, presumably once clinopyroxene crystallizes (Fig. 6d).

To estimate the composition of the transporting melt the olivine and chromite phenocrysts must be subtracted from each sample. This was done by using the average olivine composition found in each sample and subtracting this composition in one weight percent increments from the whole rock composition until the calculated liquid composition was in equilibrium with the olivine of the observed composition, assuming

K_D ($[Mg_{liq}]$*$[Fe_{ol}]$)/($[Fe_{liq}]$*$[Mg_{ol}]$) = 0.3 (Roeder and Emslie, 1970.)

This approach required extraction of between 4 and 45 weight percent olivine along with appropriate amount of chromite (0.05 to 0.56 wt%). The calculated MgO concentrations of the transporting magmas ranged from 10 to 20 weight percent (Table 4).

4.3 Chromite Composition

4.3.1 Major Elements

Chromium, Ti, Al, Fe and Mg were determined by both microprobe and LA-ICP-MS. The results for the two methods agree within two relative percent. On the assumption that the probe data are more precise for these elements the probe data will be used, but the conclusions would be similar if the LA-ICP-MS data were used.

The chromites from low-Ti picrites are richer in, Al_2O_3 than the chromites from the high Ti-picrites, which are in turn richer in Al_2O_3 than the chromites from the sill (Table 2, Fig. 7a). In contrast the Cr_2O_3 of chromites from high- and low-Ti picrites cover a similar range (Fig. 7b) and Table 2. The higher Al_2O_3 content of chromites from high-Ti picrites is consistent with the higher Al_2O_3 content of the low-Ti picrite melt. Barnes and Roeder (2001) observed that chromites from intrusions from flood basalts are generally richer in Al_2O_3 than the chromites from the associated basalts, which also appears to the case for our sill chromites. The range in compositions of the chromite in equilibrium with the low and high-Ti melts (Table 4) have been calculated using SPINMELTS2 (Nikolaev et al., 2018) at 100MPa and fO_2 of ΔFMQ ~~A~~+1 and ~~A~~0 ~~FMQ~~ respectively. (The choice of fO_2 will be justified in the next section). In terms of Ti, Cr and Al the range in observed chromite compositions are similar to the range in calculated chromite compositions in equilibrium with these melts (stars on Fig. 7a and b).

The FeO_T content of the chromites of the high-Ti picrites and sill are higher than the chromites from the low-Ti picrites and correspondingly poorer in MgO (Table 2, Fig. 7c and d). The MgO and FeO_T contents calculated by SPINMELTS2 are systematically higher for MgO and lower for FeO_T than the observed compositions and the observed compositions cover a much wider range. It has long been known that Fe, Mg, Mn and Zn in chromite re-equilibrate with the mafic silicates or trapped liquid (Roeder and Campbell, 1985; Scowen et al., 1991; Barnes, 1998) whereas ions with a larger charge such as Al, Cr, and Ti are less readily disturbed. Possibly the reason for the difference between the calculated and observed chromite compositions for MgO and FeO_T is the result of the 2+ ions having re-equilibrated with olivine in the case of the inclusion chromite and with the melt in the case of the matrix chromite.

The interpretation that Fe and Mg have re-equilibrated whereas Cr, Al and Ti have not is enforced by the observation that the FeO_T and MgO content of the inclusion and matrix chromites are significantly different with inclusion chromites being richer in MgO and poorer in FeO_T (Table 2, Fig. 8a and ESM 2 Fig 1). In contrast there is no significant difference in Cr_2O_3, Al_2O_3 and TiO_2 contents of inclusion chromites and matrix chromites (Table 2, Fig. 9a and b and ESM 2 Fig. 2). This interpretation is also consistent with the observation that 3+ and 4+ ions diffuse more slowly in chromite than 2+ ions (Coulthard et al., 2021).

4.3.2 Minor and Trace Elements

In a previous LA-ICP-MS study with conditions optimized for the determination of PGE Arguin et al. (2016) reported results for Os, Ir, Ru and Rh. In the current study PGE were also determined (Table 3) and Os, Ir, Ru and Rh found to be present at similar levels to those reported by Arguin et al. (2016). Palladium, Re, Pt and Au concentrations were found to present at less than detection limits of 10 to 30 ppb (Table 3). Molybdenum, Y, Cd, In, W and Bi were also determined, and the results are above detection limits but less than limits of quantification (Table 3). None of the above elements will be considered any further in our study.

The elements that could be quantified by LA-ICP-MS are; Al, Mg, Cr, Fe, Sc, V, Ti, Mn, Co, Ni, Cu, Zn, Ga, Nb, Sn, Hf and Ta. The Al, Mg, Cr and Fe contents of the chromites have been discussed above. Consistent with the whole rock chemistry, the chromites from high-Ti picrites are enriched in Ti, Nb, Sn, Hf, and Ta relative to chromites from the low-Ti picrites (Fig. 10a to e, Table 3). Despite having similar whole rock values for V, the V concentrations in chromites from the low-Ti picrites is generally lower than V concentrations in chromites from the high-Ti picrites (Fig. 10f, Table 3). Manganese, Co, Ni, Zn Sc and Ga contents are similar in chromites from both types of picrites (Fig. 11a to f, Table 3).

There is no significant difference in concentrations of the 3+, 4+ and 5+ ions, Ti, Sc, V, Ga, Nb, Sn and Hf between inclusion chromites and matrix chromites (Table 3, Fig. 9b to f, ESM 2 Fig. 2) . In contrast, some 2+ ions do show differences with inclusion chromites being poorer in Mn and Zn than matrix chromites and some inclusion chromites from Hi-Ti picrites being enriched in Co (Table 3 Fig. 8 c to d). Nickel does not show any significance between inclusion and matrix chromite (ESM 2 Fig. 1b).

Copper concentrations vary widely from 10 ppm to 300 ppm with no systemic pattern. The possibility that the Cu concentrations are an analytical artefact was considered. However, there is no correlation with elements that could potentially interfere with Cu such as Ti. The time-resolved spectra for Cu in chromite grains with high Cu values do not show peaks as might be expected if Cu-rich inclusions were present. In addition, higher Cu values were found both in this LA-ICP-MS study and in the study by Arguin et al. (2016) when the analytical conditions were different. We therefore conclude that Cu is indeed present at up to 300 ppm in some chromite grains. The Cu content of the high and low-Ti picrites are similar at ~ 100 ppm Cu and the chromites from both low-Ti and high-Ti picrites and show similar ranges in Cu thus the composition of the melt does not appear to be important. The presence of Cu enrichment at the edge of the chromite grains observed on the maps (Fig. 2 and 3) may provide an explanation. If the section chromite exposed in the polish section happened to expose mainly the edge of chromite then the time resolved analysis spectrum may appear homogeneous and high. Possibly Cu was present in a boundary layer at the edge of growing chromite and was incorporated in this manner.

4.4 Oxygen fugacity

There is no significant difference in $Fe^{3+}/\Sigma Fe$ of chromite grains from high-Ti picrites and chromite grains from low-Ti picrites (averages 0.26 +/-0.04 and 0.24 +/-0.04 respectively Table 2) with grains from both types of picrites covering the full range (Fig. 12a~~A~~). The range indicates a fO_2 of approximately ΔFMQ 0 to -1.4 ~~-1.4 to 0 ΔFMQ~~ (Ballhaus et al., 1991). ~~-~~ with no difference between the two types of picrite. In contrast, the V oxybarometer gives higher fO_2 and shows a difference between low- and high-Ti picrites.

Based on the V oxybarometer the fO_2 was calculated using the equation from Canil (2002)

$$\Delta NiNiO = \{\log[(V_{liq}/V_{chr})*24.1\text{-}1]\text{-}0.82\}/0.28$$

This equation requires the V content of the liquid (V_{liq}) and chromite (V_{chr}). As mentioned above, the whole rock compositions do not represent liquid compositions and needs to be recalculated to remove the olivine and chromite phenocrysts. The liquid compositions were estimated as described above. The chromites from low-Ti picrites have higher fO_2 than the chromites from high-Ti picrites (Fig. 12b~~B~~) averaging at ΔNiNiO at +0.19 and ΔNiNiO at -0.57 respectively. These fO_2 are equivalent of ΔF~~Q~~MQ +0.88 and +0.12 (http://www.kaylaiacovino.com/tools-for-petrologists).

4.5 Partition Coefficients

Whereas, we accept the chromites may not have crystallized from the transporting melt, that is to say they could be antecrysts, it also is possible that they did crystallize from the transporting melt and that empirical partition coefficients can be estimated using the calculated melt compositions. Average partition coefficients are listed in Table 5 using the recalculated melt concentrations. Also shown are the partition coefficients for the samples where the smallest

correction to the whole rock composition was necessary (4% olivine and 0.05% chromite removal for sample BC-04 for low-Ti picrite, and 17% olivine and 0.20 % chromite removal for sample JC-07 for the high-Ti picrite). The partition coefficients for these two samples agree with the average partition coefficients indicating that calculation to estimate the melt compositions has not distorted the estimated partition coefficients.

The partition coefficients for the 3+. 4+ and 5+ ions are generally similar to the partition coefficients calculated for chromites and Cr-spinels using the experiments run between Δ FMQ −2 ~~FMQ~~ to Δ+2 ~~FMQ~~ (Table 5). The 3+ site is mainly occupied by Cr and those ions with radii within 15 % of the radius of Cr^{3+}, (V, Ga and Al) have partition coefficients between 1 and 4. Scandium and In are also 3+ ion, but are slightly too large to substitute for Cr^{3+} and the partition coefficients are therefore lower at approximately 0.2 and <0.5, respectively. The partition coefficients for Ga, Al and Sc are not significantly different between chromites from high- and low-Ti picrites or between chromites in the matrix and chromites in the olivine phenocrysts (Table 5). In contrast the V partition coefficient for the chromites from low-Ti picrites are lower than those from high-Ti picrites. We interpret this to be a result of lower fO_2 in the high-Ti picrites and consequently more of the V is in the 3+ state and can more readily substitute for Cr^{3+}.

The partition coefficients for the 4+ and 5+ ions Ti, Sn, Hf, Nb and Ta range from a high of 0.8 for Ti to a low of 0.005 for Nb and Ta. The radius of Ti^{4+} is very close to that of Cr^{3+} and hence despite the difference in charge the partition coefficient is only slightly below one. There is a significant difference between the partition coefficient for Ti into chromites from high- and low-Ti picrites, with partition coefficient being significantly lower in low-Ti picrites than high Ti-picrites (0.5 vs 0.8, respectively). The Ti^{4+} substitution into the Cr^{3+} site is a coupled

substitution consisting of Ti^{4+} and Fe^{2+} (Minin et al., 2011). The higher partition coefficient of Ti into the high-Ti picrite chromite could be because the high-Ti picrite melt was richer in FeOT and thus more FeO was available. Tin and Hf have lower partition coefficients than Ti (0.2 and 0.02, respectively) probably because the differences in radii between Cr^{3+} and these elements are much larger than that of Ti. Although, Nb and Ta have similar radii to Cr^{3+} the partition coefficients are very low at approximately 0.005, reflecting the 2+ charge difference.

The empirical partition coefficients for the 2+ ions Mg, Ni, Co and Cu do not agree with the experimental determinations. Magnesium, Ni and Co partition coefficients are all slightly lower than the experimental determinations and Cu are higher. As discussed above 2+ ions may have re-equilibrated after the chromite crystallized and the lower partition coefficients could reflect this re-equilibrium. The range in partition coefficients for Cu is much wider than for the other elements and may be the result of an overestimation of the Cu content in some grains due to the boundary layer effect as discussed above.

5. Comparison with chromites from other settings.

Kamenetsky ~~Kamenetsky~~ et al. (2001) proposed a plot of TiO_2 versus Al_2O_3 to distinguish chromite from lavas of different tectonic settings. We have added a field for chromite from komatiites based on the 677 samples from the GEOROC data base. The field outlined represents the contour to include 90% of the analyses. This field overlaps with the chromites from island arc tholeiites. None of the Emeishan chromites plot in the proposed LIP field. The chromites from low-Ti picrites plot towards the edge of the komatiite and MORB fields (Fig. 13). The chromites from the high-Ti picrites plot in the ocean island basalt field (Fig. 13).

Formatted: Font: (Default) Times New Roman, 12 pt

In order to make a comparison using a wider range of trace elements we have plotted the chromites normalized to trace elements in our komatiite chromite (AX 37). This chromite is from the Alexo komatiite flow, which is from an Al-undepleted komatiite that has experienced only prehnite-pumpellyite metamorphism (Jolly, 1982) and thus the effects of metamorphism should be limited. The whole rock trace element patterns from this komatiite flow show slight depletion in LREE, Nb, Ta and Th relative to HREE, indicating the magma was from a slightly depleted mantle source (Barnes, 1985). On the chromite-normalized plots the elements are plotted in order of their compatibility with crystallization of 99 % olivine and 1 % chromite, approximately cotectic proportions from a primitive magma (Roeder et al., 2006). From Ni to Zn (from right to left), the phase controlling the elements should be olivine. From Cr to Al, the phase controlling the elements should be chromite. Titanium and Sc could show the influence of pyroxene. For Sn, and Hf the elements should be controlled by the liquid composition.

The pattern of the chromites from low-Ti picrites normalized to komatiite chromite is relatively flat with most elements in the 0.3 to 3 times komatiite range (Fig. 14a). All of the samples exhibit a positive Ti anomaly at approximately twice to thrice the komatiite value and a similar enrichment in Hf. Some grains show a depletion in Sc and enrichments in Fe, Mn and Ni. The patterns for chromites from the high-Ti picrites are more variable at 0.4 to 12 times komatiite. They have larger positive Ti anomalies with Ti in the 6 to 10 times komatiite chromite and are more enriched in Hf, Sn, Ga and V at 2 to 5 times komatiite values. As is the case for the low-Ti picrites they are slightly enriched in Mn and Ni (Fig. 14b)

The World's largest PGE resource is the UG-2 chromite-rich layer from the Bushveld Complex. It is argued that the Bushveld Complex is the product of a mantle plume (Hatton ~~and Schweitzer~~ 1995; Barnes and Maier, 2002, Florentini et al., 2020) and hence the magmas that

formed the deposit could show similarities with LIP magmas. Therefore, we compare with the recent analyses from Langa et al. (2021) for the UG-2 of the western limb (UG-2W) of the Bushveld Complex and the chromite-rich layer of the northern limb (assumed to be similar to the UG-2) hereafter referred to as UG-2N with komatiite chromite and the chromite from the Emeishan LIP.

The UG-2W and UG-2N chromite patterns normalized to komatiite are relative flat but have large positive Ti, Ga, V and Zn anomalies at up to 6 times komatiite chromite, and are depleted in Mg (Fig. 14c and d). The enrichment of Ti, Ga, V and Zn and depletion of Mg in the UG-2 chromites indicates that the magma with which they equilibrated was more evolved than a komatiite.

The UG-2 chromite patterns show some similarities with the chromites from high-Ti picrites. In order to compare the UG-2W and UG-2N layers with the composition of the chromite from high-Ti picrite, more closely the samples have been normalized to the JC-07 chromite (the sample with highest estimation of MgO content of the high-Ti picrites; (Fig.14 e and f). The UG-2W chromites are enriched in V and Zn and slightly depleted in Sc, Ti, Mg, and Ni. The UG-2N chromites have similar patterns except that V is not as enriched and they are slightly enriched in Co, Fe, Mn.

The UG-2W and UG-2N chromites are cumulate, and thus the compositions could have been modified by post-cumulate processes such as equilibration with trapped liquid. Langa et al. (2021) observed that the UG-2N chromite layer contains more interstitial silicate component than the UG-2W and argued that the UG-2N chromites have undergone equilibration with a larger trapped liquid component than the UG-2W. Thus, the higher Co, Mn, Fe and Zn observed in the

UG-2N chromite could be interpreted as the product of post-cumulate reaction with a trapped liquid.

The depletion of Sc and Ti and enrichment of V, in both the UG-2W and UG-2N chromites is more difficult to explain by equilibration with trapped liquid fraction as these elements diffuse more slowly (Coulthard, al. 2021). Also, as observed in our study of the Emeishan chromites the concentrations of these elements in the inclusion chromites and matrix chromites are similar, which we interpret to be because they diffuse more slowly. The depletion in Sc and Ti in the Bushveld chromites may reflect the effect of pyroxene crystallization as interstitial orthopyroxene is present in the case of the UG-2 chromites, thus pyroxene may have been crystallizing at the same time as chromite and competed for these elements.

Langa et al. (2021) found that $Fe^{3+}/\Sigma Fe$ is lower (0.21 to 0.23) in the chromites from the UG-2W than in chromites from UG-2N (0.23 to 0.25), which they interpret to be because the UG-2W magma was more reduced than UG-2N magma. They further argue that the northern limb rocks show evidence of *in situ* contamination by the country rocks, which could be the source of the higher oxidation. The enrichment in V in the UG-2W chromites relative to the UG-2N chromites is consistent with this argument because a more reduced magma would contain more V^{3+} which could more readily substitute into chromite. Assuming the liquid contained 200 ppm V (based on the composition of the chill zones of the Bushveld Complex, (Barnes et al., 2010) the fO_2 for the UG-2W can be estimated as approximately ΔFMQ -2 ~~ΔFMQ~~ and that of UG-2N as approximately ΔFMQ -1 ~~ΔFMQ~~. These estimates are somewhat lower than suggested by the $Fe^{3+}/\Sigma Fe$ found by Langa et al. (2021) of ΔFMQ -1 ~~ΔFMQ~~ to ~~FMQ~~ 0. However, Adetunji et al. (2013) report lower $Fe^{3+}/\Sigma Fe$ from UG-2 chromites from the eastern limb of the Bushveld (0.17 to 0.2) consistent with the lower estimation of fO_2 from V. They further showed that the

450 $Fe^{3+}/\Sigma Fe$ of the chromites was affected by subsolidus processes. Given that Fe concentrations
451 appear to be readily affected by subsolidus diffusion and as shown above V appears to
452 undergone less re-equilibration than Fe in the case of the Emeishan chromites we conclude that
453 ~~that~~ V is probably a more reliable indicator of the fO_2 than $Fe^{3+}/\Sigma Fe$.
454
455 **6 Conclusions**
456 The concentrations of 3+, 4+ and 5+ ions (Al, Ti, Sc, V, Ga, Nb, Sn, and Hf) in chromites
457 from high- and low-Ti picrites from the Emeishan Large Igneous Province are different. The
458 chromites from high-Ti picrites have higher concentrations of Ti, V, Nb, Sn and Hf than the
459 chromites from low-Ti picrites. The chromites from low-Ti picrites are enriched in Al. These
460 differences reflect the difference in the magma compositions, except for V. Whole-rock
461 concentrations of V in both high- and low-Ti picrites are similar. The higher V content in
462 chromites from the high-Ti picrites is attributed to a lower fO_2 in the high-Ti picrites resulting in
463 more of the V being present as V^{3+}.
464 The concentrations of 2+ ions Mg, Mn, Co, Ni and Zn are similar in chromite grains from
465 both high- and low-Ti picrites. The habit of the chromite grain influences the concentrations of
466 2+ ions. The chromites found in the matrix contain more Mn, Fe, and Zn than chromites included
467 in olivine. The chromites included in olivine are richer in Mg. The concentrations of 3+, 4+ and
468 5+ ions are similar in both forms of chromite. Based on the difference in the behavior of the 2+
469 and 3+, 4+, 5+ ions we consider that the 2+ ions re-equilibrated with the olivine in the case of the
470 inclusion chromite and the melt in the case of the matrix chromite.
471 Gallium, Al, V 3+ ions with radii within 15% of Cr^{3+}ions have empirical partition
472 coefficients in the 1 to 3 range indicating that they are compatible with chromite. Scandium (also

a 3+ ions) has a low partition coefficients due to its large radius. Most of the 4+ and 5+ ions (Nb, Sn, Hf, Ta) are strongly incompatible. Titanium is an exception to this with partition coefficients in the 0.5 to 0.8 range. This could be because Ti^{4+} radius is close to that of Cr^{3+}.

Relative to komatiite chromites, the Emeishan chromites are enriched in Hf, Sn, Ti, Ga, Zn and Mn. The chromites from the World's largest PGE deposit, the UG-2, show some similarities with the chromite from the Emeishan high Ti-picrites, but are more enriched in Ga, V, Zn and Fe and depleted in Sc, Ti, Mg and Ni. These enrichments and depletions suggest that the magma with which UG-2 chromite equilibrated was more evolved than the either the komatiite or Emeishan picrites.

Declaration of Competing Interest

The authors declare that they have no known competing financial interests or personal relationships that could have appeared to influence the work reported in this paper.

Acknowledgements

The anonymous reviewers are thanked for their time and efforts to clarify this work. This study was funded by the Natural Sciences and Engineering Research Council of Canada Discovery Grant 1884-2013 (S-J B). The samples were originally collected as part of an MSc project published as Arguin et al (2016) and which was funded jointly by the Canadian Research Chair in Magmatic Metallogeny grant #950-215503 (S-JB) and State Key Laboratory of Ore Deposit Geochemistry of China: SKLODG grant #201204 to Dr. Xie-Yan Song. Dr. Song-Yue Yu is thanked for help in collection of the samples for the original study.

References

Adetunji, J., Everitt, S., Rollinson, H., 2013. New Mössbauer measurements of Fe3+/ΣFe ratios in chromites from the early Proterozoic Bushveld Complex, South Africa. Precambrian Research 228, 194-205.

Ali, J.R., Thompson, G.M., Zhou, M.-F., Song, X., 2005. Emeishan large igneous province, SW China. Lithos 79, 475-489.

Arguin, J.-P., Pagé, P., Barnes, S.-J., Yu, S.-Y., Song, X.-Y., 2016. The effect of chromite crystallization on the distribution of osmium, iridium, ruthenium and rhodium in picritic magmas: an example from the Emeishan Large Igneous Province, Southwestern China. Journal of Petrology 57, 1019-1048.

Bai M.., Hong, Z., Weiguang, Z., Zhongjie, B., Defeng, H., 2013. Platinum- Group Element Geochemical Characteristics of the Picrites and High- Ti Basalts in the Binchuan Area, Yunnan Province. Acta Geologica Sinica- English Edition 87, 158-175.

Ballhaus, C., Berry, R.F., Green, D.H., 1991. High pressure experimental calibration of the olivine-orthopyroxene-spinel oxygen geobarometer: implications for the oxidation state of the upper mantle. Contributions to Mineralogy and Petrology 107, 27-40.

Barnes, S.J., 1998. Chromite in komatiites, 1. Magmatic Controls on Crystallization and Composition. Journal of Petrology 39, 1689-1720.

Barnes, S.J., Roeder, P.L., 2001. The range of spinel compositions in terrestrial mafic and ultramafic rocks. Journal of Petrology 42, 2279-2302.

Barnes, S.-J., 1985. The petrography and geochemistry of komatiite flows from the Abitibi Greenstone Belt and a model for their formation. Lithos 18, 241-270

Formatted: Font: (Default) Times New Roman, 12 pt

Formatted: Font: (Default) Times New Roman, 12 pt, English (United States)

Barnes, S-J., Maier, W.D., 2002. Platinum-group element distributions in the Rustenburg layered suite of the Bushveld Complex, South Africa, The Geology, Geochemistry, Mineralogy and Mineral Beneficiation of Platinum-group Elements. ~~ed L.J Cabri~~ Canadian Institute of Mining, Metallurgy and Petroleum Special Vol 57 ed L.J Cabri~~,~~ pp. 431-458.

Barnes, S.-J., Maier, W.D., Curl, E.A., 2010. Composition of the marginal rocks and sills of the Rustenburg Layered Suite, Bushveld Complex, South Africa: implications for the formation of the platinum-group element deposits. Economic Geology 105, 1491-1511.

Bédard, J.H., 2005. Partitioning coefficients between olivine and silicate melts. Lithos 83, 394-419.

Brenan, J.M., Finnigan, C.F., McDonough, W.F., Homolova, V., 2012. Experimental constraints on the partitioning of Ru, Rh, Ir, Pt and Pd between chromite and silicate melt: the importance of ferric iron. Chemical Geology 302, 16-32.

Canil, D., 2002. Vanadium in peridotites, mantle redox and tectonic environments: Archean to present. Earth and Planetary Science Letters 195, 75-90.

Canil, D., Fedortchouk, Y., 2001. Olivine–liquid partitioning of vanadium and other trace elements, with applications to modern and ancient picrites. The Canadian Mineralogist 39, 319-330.

Chen, L.-M., Song, X.-Y., Hu, R.-Z., Yu, S.-Y., He, H.-L., Dai, Z.-H., She, Y.-W., Xie, W., 2017. Controls on trace-element partitioning among co-crystallizing minerals: Evidence from the Panzhihua layered intrusion, SW China. American Mineralogist 102, 1006-1020.

Coulthard, D.A., Zellmer, G.F., Tomiya, A., Jégo, S., Brahm, R., 2021. Petrogenetic implications of chromite-seeded boninite crystallization experiments: Providing a basis for chromite-

Formatted: Font: (Default) Times New Roman, 12 pt

Formatted: Font: (Default) Times New Roman, 12 pt, English (United States)

Formatted: Font: (Default) Times New Roman, 12 pt

Formatted: Font: (Default) Times New Roman, 12 pt, English (United States)

Formatted: Font: (Default) Times New Roman, 12 pt

melt diffusion chronometry in an oxybarometric context. Geochimica et Cosmochimica Acta 297, 179-202.

Fiorentini, M.L., O'Neill, C., Giuliani, A., Choi, E., Maas, R., Pirajno, F., Foley, S., 2020. Bushveld superplume drove Proterozoic magmatism and metallogenesis in Australia. Scientific Reports 10, 1-10.

Frost, B.R., 1991. Introduction to oxygen fugacity and its petrologic importance. Reviews in Mineralogy and Geochemistry 25, 1-9.

Garuti, G., Evgeny, E.V., Thalhammer, O.A., Zaccarini, F., 2012. Chromites of the Urals (Part 1: Overview of chromite mineral chemistry and geo-tectonic setting. Ofioliti 37, 27-53.

González-Jiménez, J.M., Griffin, W.L., Proenza, J.A., Gervilla, F., O'Reilly, S.Y., Akbulut, M., Pearson, N.J., Arai, S., 2014. Chromitites in ophiolites: How, where, when, why? Part II. The crystallization of chromitites. Lithos 189, 140-158.

Hanski, E., Kamenetsky, V.S., Luo, Z.-Y., Xu, Y.-G., Kuzmin, D.V., 2010. Primitive magmas in the Emeishan Large Igneous Province, southwestern China and northern Vietnam. Lithos 119, 75-90.

Hatton, C.J., 1995. Mantle plume origin for the Bushveld and Ventersdorp magmatic provinces. Journal of African Earth Sciences 21, 571-577.

Horn, I., Jenner, G., 1994. Compositional dependencies of the partition coefficients for Zr, Nb, Ta, Hf and selected transition elements between spinel and melt. Geochim. Cosmochim. Acta 51, 1071-1081.

Irvine, T., 1975. Crystallization sequences in the Muskox Intrusion and other layered complexes-origin of chromitite layers and similar deposits of other magmatic ores. Geochimica et Cosmochimica Acta 39, 921-1020.

Jenkins, M.C., Mungall, J.E., 2018. Genesis of the peridotite zone, Stillwater Complex, Montana, USA. Journal of Petrology 59, 2157-2189.

Jolly, W.T., 1982. Progressive metamorphism of komatiites and related Archean laas of the Abitibi area, Canada. In: Komatiites (N. T. Arndt & E. G. Nisbet, eds.). Geoge Allen and Unwin, London, U.K.

Kamenetsky, V.S., Crawford, A.J., Meffre, S., 2001. Factors controlling chemistry of magmatic spinel: an empirical study of associated olivine, Cr-spinel and melt inclusions from primitive rocks. Journal of Petrology 42, 655-671.

Kamenetsky, V.S., Chung, S.-L., Kamenetsky, M.B., Kuzmin, D.V., 2012. Picrites from the Emeishan Large Igneous Province, SW China: a compositional continuum in primitive magmas and their respective mantle sources. Journal of Petrology 53, 2095-2113.

Langa, M.M., Jugo, P.J., Leybourne, M.I., Grobler, D.F., Adetunji, J., Skogby, H., 2021. Chromite chemistry of a massive chromitite seam in the northern limb of the Bushveld Igneous Complex, South Africa: correlation with the UG-2 in the eastern and western limbs and evidence of variable assimilation of footwall rocks. Mineralium Deposita 56, 31-44.

Latyshev, A., Rad'ko, V., Veselovskiy, R., Fetisova, A., Pavlov, V., 2020. Correlation of the Permian-Triassic ore-bearing intrusions of the Norilsk region with the volcanic sequence of the Siberian Traps based on the paleomagnetic data. Economic Geology 115, 1173-1193.

Li, C., Tao, Y., Qi, L., Ripley, E.M., 2012. Controls on PGE fractionation in the Emeishan picrites and basalts: constraints from integrated lithophile–siderophile elements and Sr–Nd isotopes. Geochimica et Cosmochimica Acta 90, 12-32.

Formatted: Font: (Default) Times New Roman, 12 pt, English (United States)

Formatted: Font: (Default) Times New Roman, 12 pt

588 Li, J., Wang, X.-C., Ren, Z.-Y., Xu, J.-F., He, B., Xu, Y.-G., 2014. Chemical heterogeneity of
589 the Emeishan mantle plume: evidence from highly siderophile element abundances in
590 picrites. Journal of Asian Earth Sciences 79, 191-205.
591 Longerich, H.P., Jackson, S.E., Günther, D., 1996. Inter-laboratory note. Laser ablation
592 inductively coupled plasma mass spectrometric transient signal data acquisition and
593 analyte concentration calculation. Journal of Analytical Atomic Spectrometry 11, 899-
594 904.
595 Locmelis, M., Pearson, N.J., Barnes, S.J., Fiorentini, M.L., 2011. Ruthenium in komatiitic
596 chromite. Geochimica Cosmochimica Acta 75, 3645-3661.
597 Maier, W.D., Barnes, S.-J., Karykowski, B., 2016. A chilled margin of komatiite and Mg-rich
598 basaltic andesite in the western Bushveld Complex, South Africa. Contributions to
599 Mineralogy and Petrology 171, 57.
600 Minin, V., Prugov, V., Podgornykh, N., Kovyazin, S., Kholodova, L., 2011. Composition of
601 chromites from kimberlites of the Botuobinskaya pipe in Yakutia. Geology of Ore
602 Deposits 53, 626-638.
603 Naldrett, A.J., Wilson, A., Kinnaird, J., Yudovskaya, M., Chunnett, G., 2012. The origin of
604 chromitites and related PGE mineralization in the Bushveld Complex: new mineralogical
605 and petrological constraints. MIneralium Deposita 47, 209-232.
606 Nicklas, R.W., Puchtel, I.S., Ash, R.D., 2016. High-precision determination of the oxidation
607 state of komatiite lavas using vanadium liquid-mineral partitioning. Chemical Geology
608 433, 36-45.
609 Nikolaev, G. S., Ariskin, A. A., Barmina, G. S., 2018. SPINMELT-2.0: Simulation of spinel–
610 melt equilibrium in basaltic systems under pressures up to 15 kbar: II. Description of the

Formatted: Font: (Default) Times New Roman, 12 pt, English (United States)

Formatted: Font: (Default) Times New Roman, 12 pt

611 program package, the topology of the Cr-spinel–melt model system, and petrological
612 implications. Geochemistry International 56, 125–135.
613 Nixon, G.T., Cabri, L.J., Laflamme, G.J.H., 1990. Platinum-group element mineralization in lobe
614 and placer deposits associated with the Tulameen Alaskan-type Complex, British
615 Columbia. Canadian Mineralogist 28, 503-535.
616 Pagé, P., Barnes, S.-J., 2009. Using trace elements in chromites to constrain the origin of
617 podiform chromitites in the Thetford Mines ophiolite, Québec, Canada. Economic
618 Geology 104, 997-1018.
619 Paton, C., Hellstrom, J., Paul, B., Woodhead, J., Hergt, J., 2011. Iolite: Freeware for the
620 visualisation and processing of mass spectrometric data. Journal of Analytical Atomic
621 Apectrometry 26, 2508-2518. 26, 2508-2518.
622 Righter, K., Campbell, A.J., Humayun, M., Hervig, R.L., 2004. Partitioning of Ru, Rh, Pd, Re, Ir
623 and Au between Cr-bearing spinel, olivine, pyroxene and silicate melts. Geochimica and
624 Cosmochimica Acta 68, 867-880
625 Roeder, P.L., Emslie, R.F., 1970. Olivine-liquid equilibrium. Contributions to Mineralogy and
626 Petrology 29, 275-289.
627 Roeder, P.L., Campbell, I.H., 1985. The effect of postcumulus reactions on composition of
628 chrome-spinels from the Jimberlana intrusion. Journal of Petrology 26, 763-786.
629 Roeder, P., Gofton, E., Thornber, C., 2006. Cotectic proportions of olivine and spinel in olivine-
630 tholeiitic basalt and evaluation of pre-eruptive processes. Journal of Petrology 47, 883-
631 900.
632 Scowen, P., Roeder, P., Helz, R.T., 1991. Reequilibration of chromite within Kilauea Iki lava
633 lake, Hawaii. Contributions to Mineralogy and Petrology 107, 8-20.

634 Shellnutt, J.G., 2014. The Emeishan large igneous province: A synthesis. Geoscience Frontiers 5,
635 369-394.
636 Solovova, I., Yudovskaya, M., Kinnaird, J., Wilson, A., Zinovieva, N., 2021. A siliceous
637 komatiitic source of Bushveld magmas revealed by primary melt inclusions in olivine.
638 Lithos 388, 106094.
639 Song, X.-Y., Zhou, M.-F., Hou, Z.-Q., Cao, Z.-M., Wang, Y.-l., Li, Y., 2001. Geochemical
640 Constraints on the Mantle Source of the Upper Permian Emeishan Continental Flood
641 Basalts, Southwestern, China. International Geology Review 43, 213-225.
642 Song, X.-Y., Zhou, M.-F., Cao, Z.-M., Sun, M. Wang, Y.-L., 2003. Ni-Cu-(PGE) magmatic
643 sulfide deposits in the Yangliuping area, Permian Emeishan igneous province, SW China.
644 Mineralium Deposita 38, 831-843.
645 Song, X.-Y., Zhou, M.-F., Cao, Z.-M., 2004. Genetic relationships between base-metal sulfides
646 and platinum-group minerals in the Yangliuping Ni-Cu-(PGE) sulfide deposit,
647 southwestern China. The Canadian Mineralogist 42, 469-483.
648 Song, X.-Y., Zhou, M.-F., Keays, R. R., Cao, Z.-M., Sun, M., Qi, L., 2006. Geochemistry of the
649 Emeishan flood basalts at Yangliuping, Sichuan, SW China: implications for sulfide
650 segregation. Contributions to Mineralogy and Petrology 152, 53-74.
651 Tao, Y., Li, C., Hu, R., Ripley, E. M., Du, A., Zhong, H., 2007. Petrogenesis of the Pt-Pd
652 mineralized Jinbaoshan ultramafic intrusion in the Permian Emeishan Large Igneous
653 Province, SW China. Contributions to Mineralogy and Petrology 153, 321-337.
654 Tao, Y., Li, C., Song, X.-Y., Ripley, E. M., 2008. Mineralogical, petrological, and geochemical
655 studies of the Limahe mafic-ultramafic intrusion and associated Ni-Cu sulfide ores, SW
656 China. Mineralium Deposita 43, 849-872.

657 Tao, Y., Li, C., Hu, R., Qi, L., Qu, W., Du, A., 2010. Re-Os isotopic constraints on the genesis of
658 the Limahe Ni-Cu deposit in the Emeishan large igneous province, SW China. Lithos
659 119, 137-146.
660 Tolstykh, N., Shvedov, G., Polonyankin, A., Korolyuk, V., 2020. Geochemical Features and
661 Mineral Associations of Differentiated Rocks of the Norilsk 1 Intrusion. Minerals 10,
662 688.
663 Wang, C. Y., Zhou, M.-F., 2011. Chalcophile element geochemistry and petrogenesis of high-Ti
664 and low-Ti magmas in the Permian Emeishan Large I,gneous province, SW China.
665 Contributions to Mineralogy and Petrology 161, 237-254.
666 Wang, C.Y., Zhou, M.-F., Zhao, D., 2005. Mineral chemistry of chromite from the Permian
667 Jinbaoshan Pt–Pd–sulphide-bearing ultramafic intrusion in SW China with petrogenetic
668 implications. Lithos 83, 47-66.
669 Wang, C. Y., Zhou, M.-F., Keays, R. R., 2006. Geochemical constraints on the origin of the
670 Permian Baimazhai mafic-ultramafic intrusion, SW China. Contributions to Mineralogy
671 and Petrology 152, 309-321.
672 Wang, C. Y., Zhou, M.-F., Qi, L., 2007. Permian flood basalts and mafic intrusions in the
673 Jinping (SW China)-Song Da (northern Vietnam) district: Mantle sources, crustal
674 contamination and sulfide segregation. Chemical Geology 243, 317-343.
675 Wang, C.Y., Zhou, M.-F., Zhao, D., 2008. Fe–Ti–Cr oxides from the Permian Xinjie mafic–
676 ultramafic layered intrusion in the Emeishan large igneous province, SW China:
677 crystallization from Fe-and Ti-rich basaltic magmas. Lithos 102, 198-217.

Formatted: Font: (Default) Times New Roman, 12 pt, English (United States)

Formatted: Font: (Default) Times New Roman, 12 pt

678 Wijbrans, C.H., Klemme, S., Berndt, J., Vollmer, C., 2015. Experimental determination of trace
679 element partition coefficients between spinel and silicate melt: the influence of chemical
680 composition and oxygen fugacity. Contributions to Mineralogy and Petrology 169, 45.
681 Wilson, A.H., 2012. A chill sequence to the Bushveld Complex: insight into the first stage of
682 emplacement and implications for the parental magmas. Journal of Petrology 53, 1123-
683 1168.
684 Xiao, L., Xu, Y. G., Mei, H. J., Zheng, Y. F., He, B., Pirajno, F., 2004. Distinct mantle sources
685 of low-Ti and high-Ti basalts from the western Emeishan large igneous province, SW
686 China: implications for plume-lithosphere interaction. Earth and Planetary Science
687 Letters 228, 525-546.,
688 Xu, Y., Chung, S.-L., Jahn, B.-M., Wu, G., 2001. Petrologic and geochemical constraints on the
689 petrogenesis of Permian-Triassic Emeishan flood basalts in southwestern China. Lithos
690 58, 145-168.
691 Zhang, Z. C., Mao, J., Mahoney, J. J., Wang, F., Qu, W., 2005. Platinum group elements in the
692 Emeishan large igneous province, SW China: Implications for mantle sources.
693 Geochemical Journal 39, 371-382.
694 Zhang, Z. C., Mahoney, J. J., Mao, J. W., Wang, F. S., 2006. Geochemistry of picritic and
695 associated basalt flows of the Western Emeishan flood basalt province. Journal of
696 Petrology 47, 1997-2019.
697 Zhong, H., Zhu, W. G., 2006. Geochronology of layered mafic intrusions from the Pan-Xi area
698 in the Emeishan large igneous province, SW China. Mineralium Deposita 41, 599-606.
699 Zhou, M.-F., Robinson, P. T., Lesher, C. M., Keays, R. R., Zhang, C. J., Malpas, J., 2005.
700 Geochemistry, petrogenesis, and metallogenesis of the Panzhihua gabbroic layered

Formatted: Font: (Default) Times New Roman, 12 pt, English (United States)

Formatted: Font: (Default) Times New Roman, 12 pt

intrusion and associated Fe-Ti-V-oxide deposits, Sichuan Province, SW China. Journal of Petrology 46, 2253-2280.

Zhou, M.-F., Arndt, N. T., Malpas, J., Wang, C. Y., Kennedy, A. K., 2008. Two magma series and associated ore deposit types in the Permian Emeishan large igneous province. Lithos 103, 352-368.

Zhou, M.-F., Chen, W. T., Wang, C. Y., Prevec, S. A., Liu, P. P., Howarth, G. H., 2013. Two stages of immiscible liquid separation in the formation of Panzhihua-type Fe-Ti-V oxide deposits, SW China. Geoscience Frontiers 4, 481-502.

Figure Captions

Fig. 1. Schematic geological map showing locations of sample localities for this study and the distribution of flood basalt successions in the Emeishan Province, southwestern China LMS Longmenshan thrust fault. Modified after Kamenetsky et al. (2012).

Fig. 2 Photomicrograph and element maps showing variations in element concentrations of a chromite inclusion in olivine. Chr = chromite. Note that with the exception of Cu the elements show the similar concentrations across the grain.

Fig. 3 Photomicrograph and variations in element concentrations of a chromite in the matrix. Chr=chromite, Ti-Mgt = Ti-rich magnetite, Note: a) that there is an overgrowth of Ti-rich magnetite on the chromite grain; b) with the exception of Cu the elements show the similar concentrations across the chromite grain.

Fig. 4. Whole rock concentrations of MgO vs: a) Ni, b) Co, c) MnO, d) Zn, e) FeOt, f) Cr_2O_3. FeOT = all Fe as FeO. Note those elements compatible with olivine Ni and Co show a positive correlation with MgO. Those elements with partition coefficients of approximately 1 into olivine MnO, Zn and FeOt show a flat trend. The positive correlation of MgO and Cr_2O_3 implies that in addition to olivine chromite was crystallizing.

Fig. 5 Whole rock concentrations of MgO vs a) TiO_2, b) Al_2O_3, c) Sn, d) Hf and e) Nb. All of these elements show a negative correlation with MgO consistent with olivine crystallization. The high-Ti picrites are enriched in TiO_2, Sn and Hf relative to the low-Ti picrites and poorer in Al_2O_3. The high-Ti picrites and the low-Ti Binchuan picrites are enriched in Nb relative to the Dali picrites. Literature data from Bai et al. (2014), Li et al. (2012), Li et al. (2014), Zang (2005).

731 Fig. 6 Whole rock concentrations of MgO vs a) V, b) Cu, c) Ga and d) Sc. Vanadium, Cu and Ga
732 show a negative correlation with MgO for the picrites consistent with olivine crystallization,
733 however there does not appear to be a difference in concentrations between the high-Ti and low-
734 Ti picrites. Scandium shows no clear trends. Literature data from Bai et al. (2014), Li et al.
735 (2012), Li et al. (2014), Zang (2005).

736 Fig. 7 TiO_2 vs; a) Al_2O_3; b) Cr_2O_3 c) MgO and d) FeOt concentrations in chromites. Stars show
737 the composition of the chromite as calculated by SPINMELTS2 for the melt composition of
738 highest and lowest MgO contents. These compositions cover the observed range of compositions
739 for TiO_2, versus Al_2O_3 and Cr_2O_3, however the calculated chromite compositions are contain
740 much less FeOt and much more MgO than the observed compositions.

741 Fig. 8 Comparison of a) FeOT, b) MnO, c) Co, d) Zn concentrations in inclusions and matrix
742 chromites showing that matrix chromites are enriched in FeOT, MnO and Zn.

743 Fig. 9 Comparison of a) Al2O3, b) TiO2, c) Sc, d) V, e) Ga and f) Hf concentrations in
744 inclusions and matrix chromites showing that concentrations of these elements are similar in and
745 inclusion chromites.

746 Fig. 10 Plots of whole rock concentrations versus chromite element concentrations illustrating
747 that the chromite composition reflect the differences in whole rock compositions with chromites
748 from high-Ti picrites being enriched in; a) TiO_2, b) Nb, c) Sn, d) Hf and e)Ta. In contrast V
749 concentrations in whole rock from both high and low-Ti picrites are similar but the chromites
750 from high-Ti picrites are enriched in V relative to the chromites from low-Ti picrites f).

751 Fig. 11 Plots of whole rock TiO_2 vs chromite concentrations of a) Mn, b) Co, c) Ni, d) Zn, e) Sc
752 and f) Ga showing that the concentrations of these elements in chromite from high-Ti and low-Ti
753 picrites are similar.

754 Fig. 12 a) $Fe^{3+}/\Sigma Fe$ vs TiO_2 in chromite; b) calculated fO_2 based on V content expressed as
755 ΔNNO versus TiO_2 concentrations in whole rock. Note that $Fe^{3+}/\Sigma Fe$ covers the same range in
756 all chromites indicating no difference fO_2 among chromites, whereas fO_2 calculated based on V
757 content shows that the chromites from high-Ti picrites have a lower *f*O2 than the chromites from
758 low-Ti picrites. *f*O2.

759 Fig. 13 Plot of Al_2O_3 versus TiO_2 contents of chromite to compare with the fields of chromite
760 compositions from the literature as defined by Kamenetsky et al. (2001) with the addition of a
761 field for komatiites (this work) based on GEOROC. The chromites from low-Ti picrites overlap
762 with the komatiite (kom) and arc-tholeiite fields. The chromite from high-Ti picrites overlap
763 with ocean island basalt (OIB) field. Neither plot in the large igneous province (LIP) field.

764 Fig. 14 a) to d) Composition of the Emeishan and UG-2 chromites normalized to komatiite
765 chromite with elements plotted in order of compatibility with crystallization of 99 % olivine and
766 1% chromite. a) Low-Ti picrites, b) High-Ti picrites, c) UG-2 Western limb Bushveld, d) UG-2
767 northern limb Bushveld. e) and f) Composition of UG-2 chromites normalized to chromite from
768 high-Ti picrites. UG-2 data from Langa et al. (2021).

769

772

Figure 1

Click here to access/download;Figure;fig 1.pdf

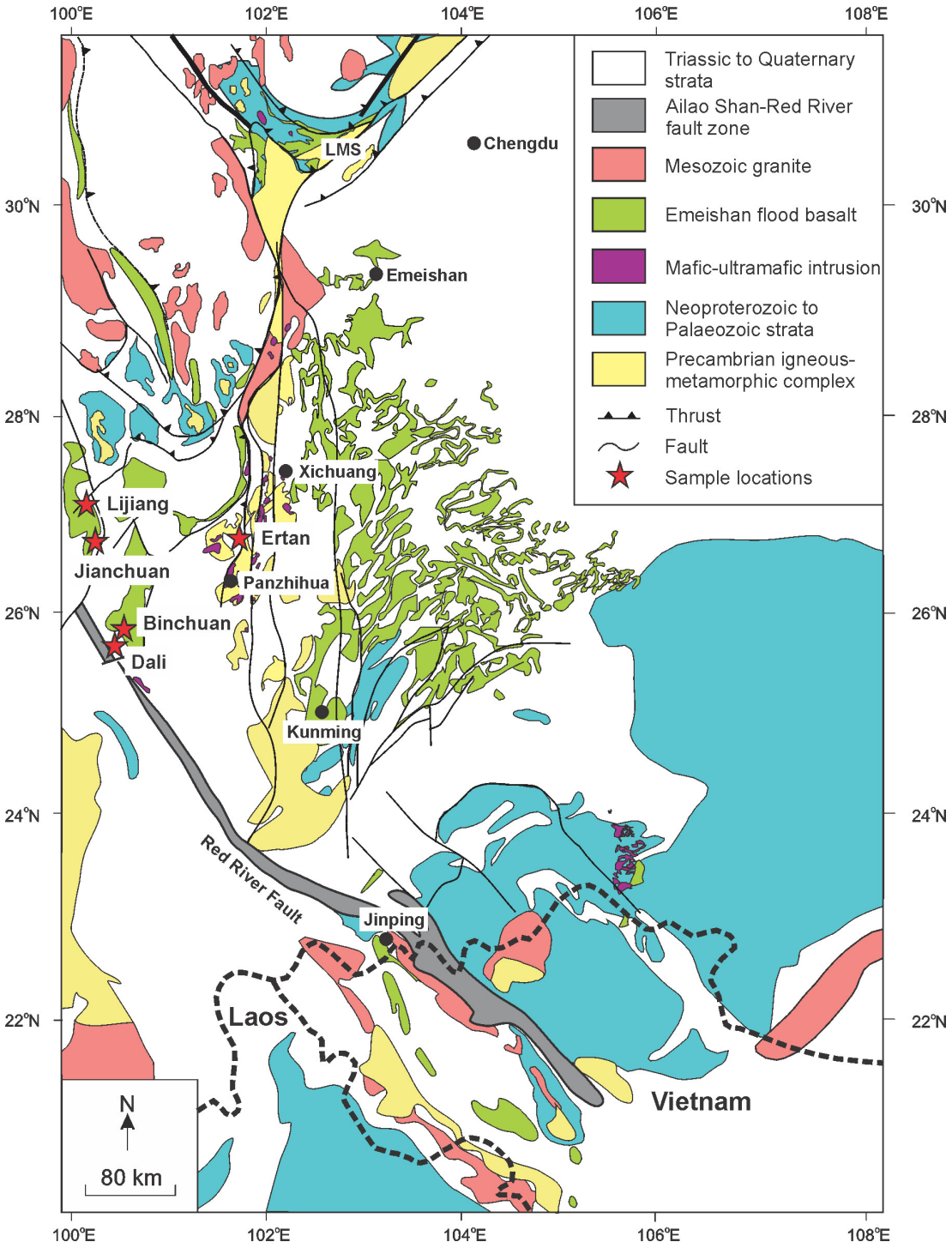

Figure 2

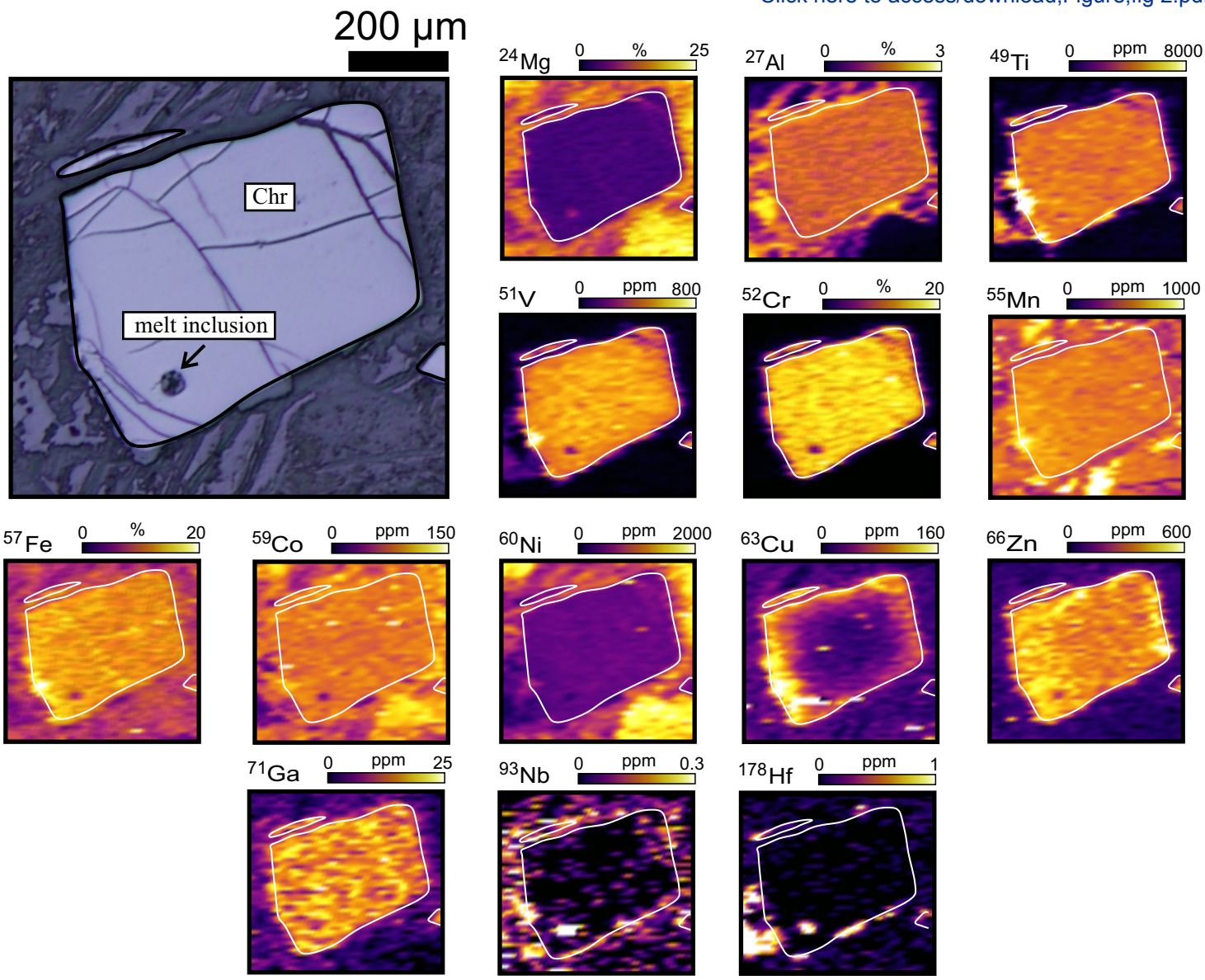

Figure 3

Click here to access/download;Figure;fig 3r.pdf

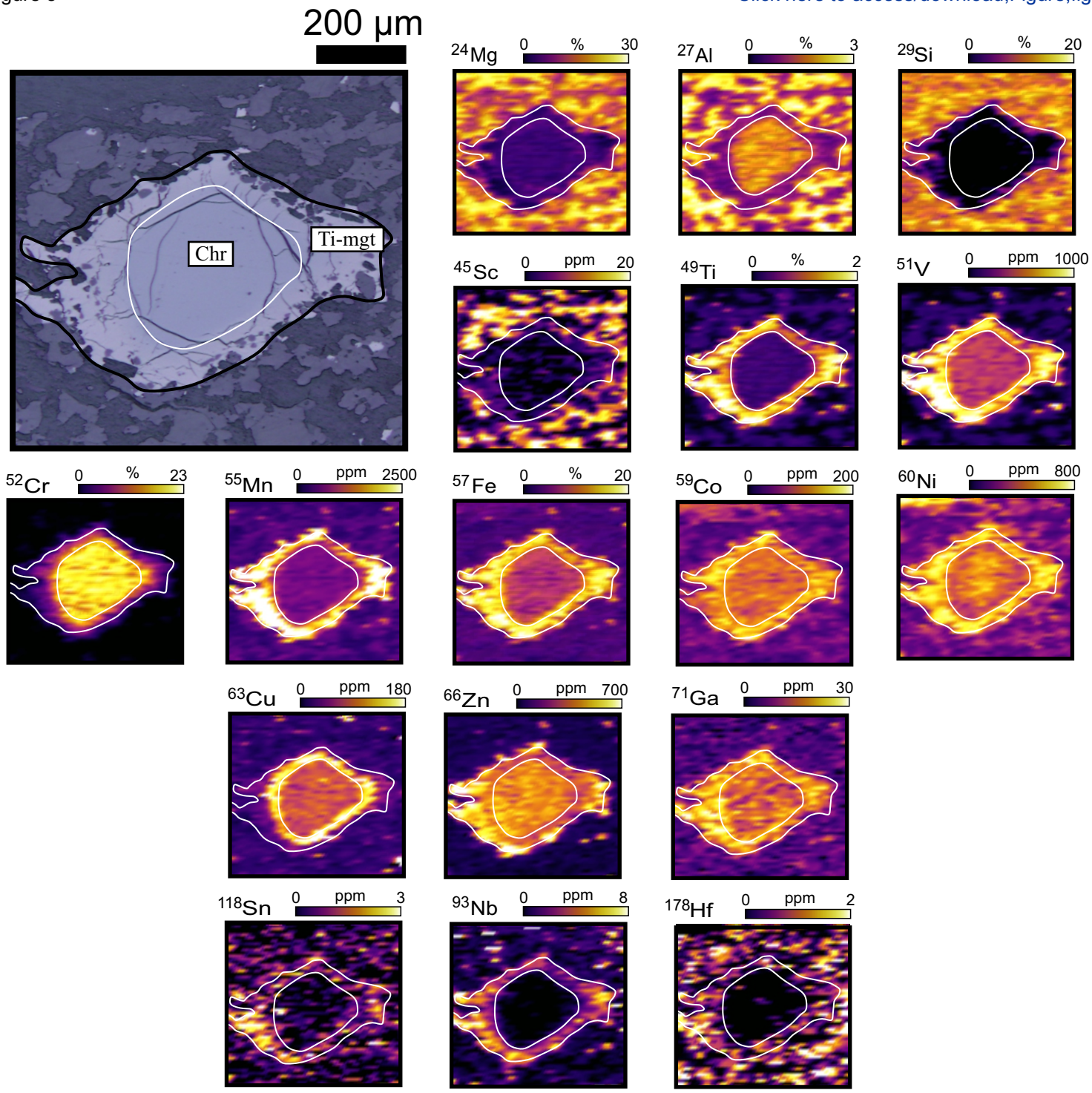

Figure 4

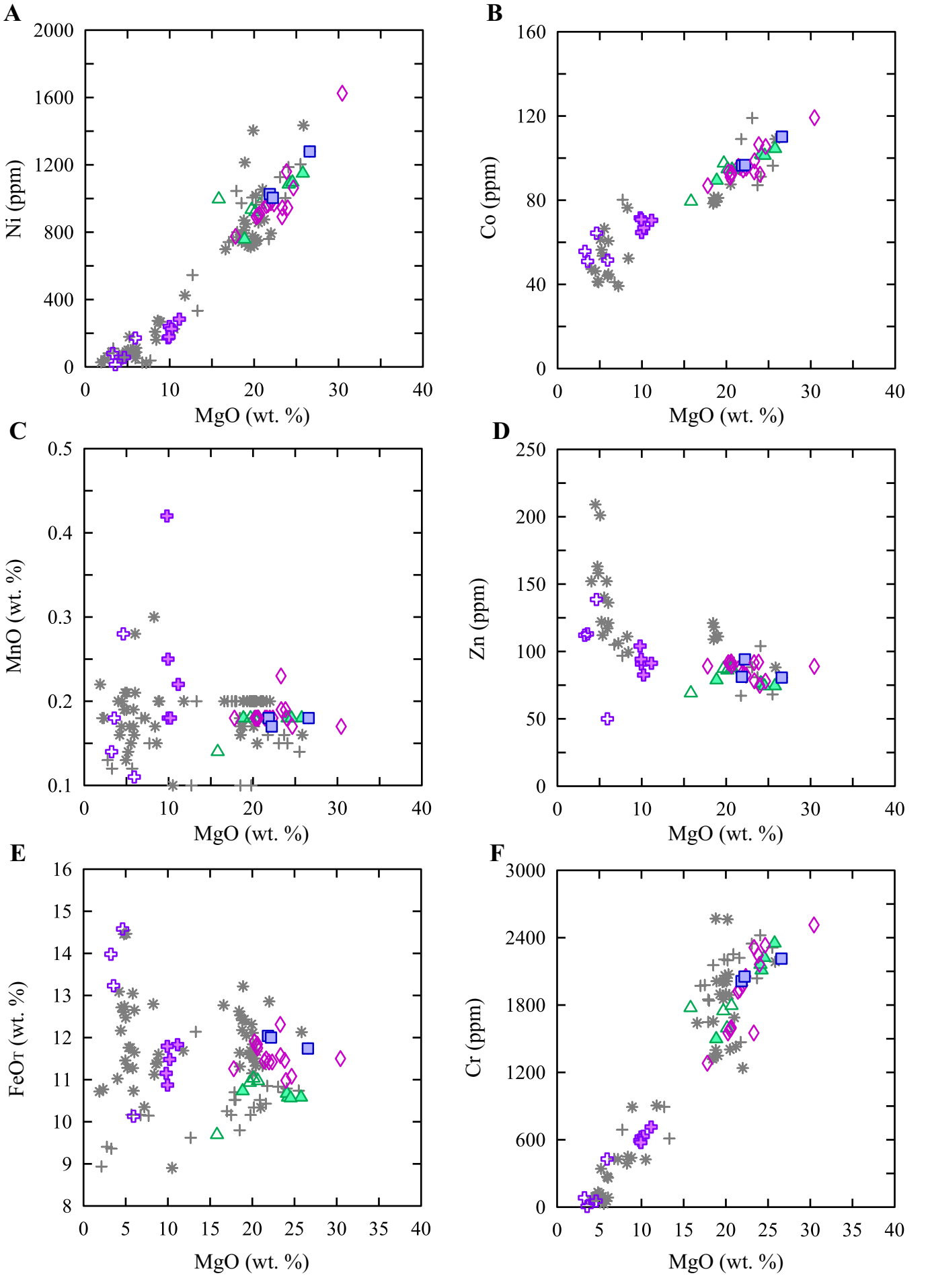

Figure 5

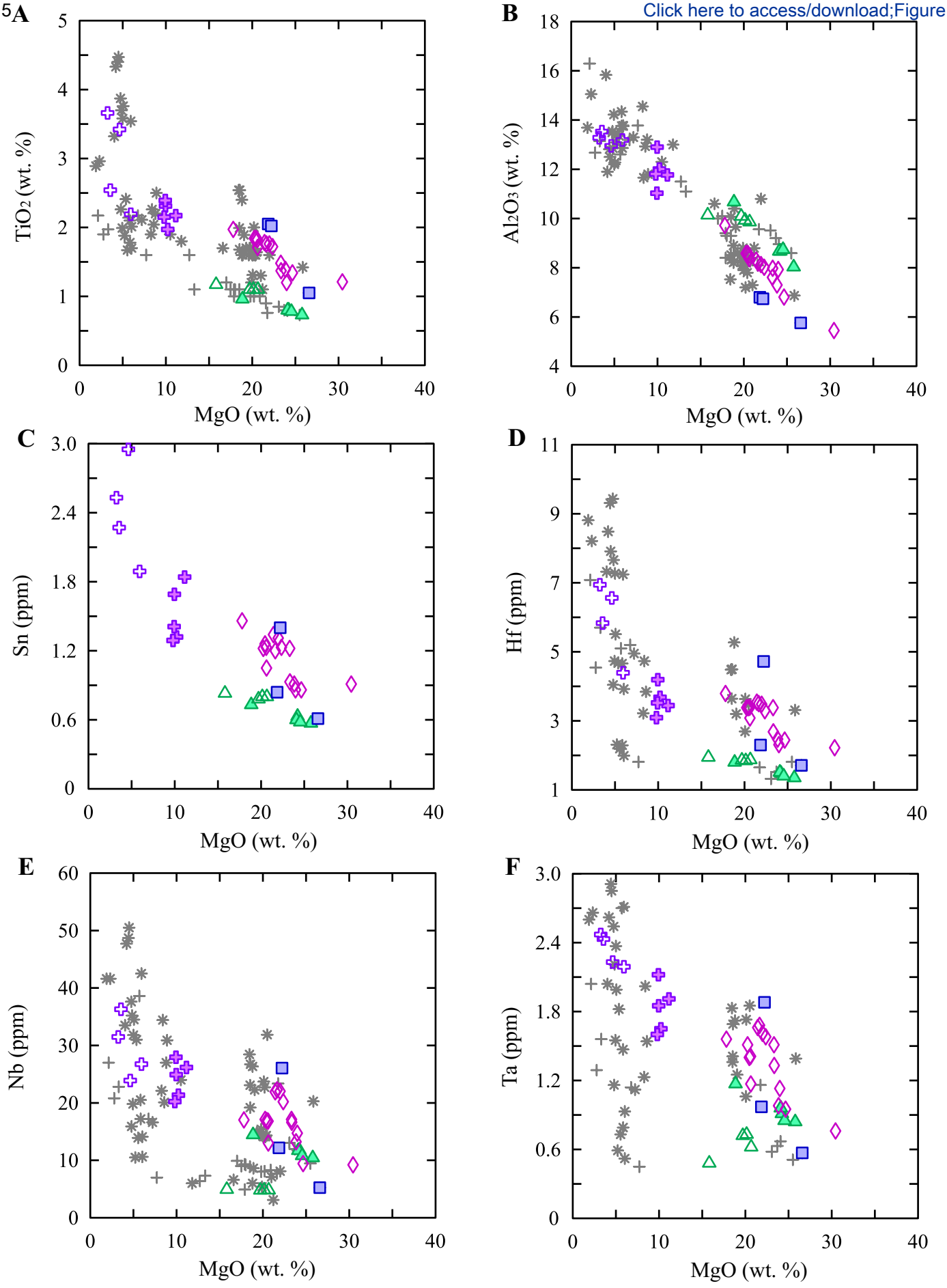

Figure 6

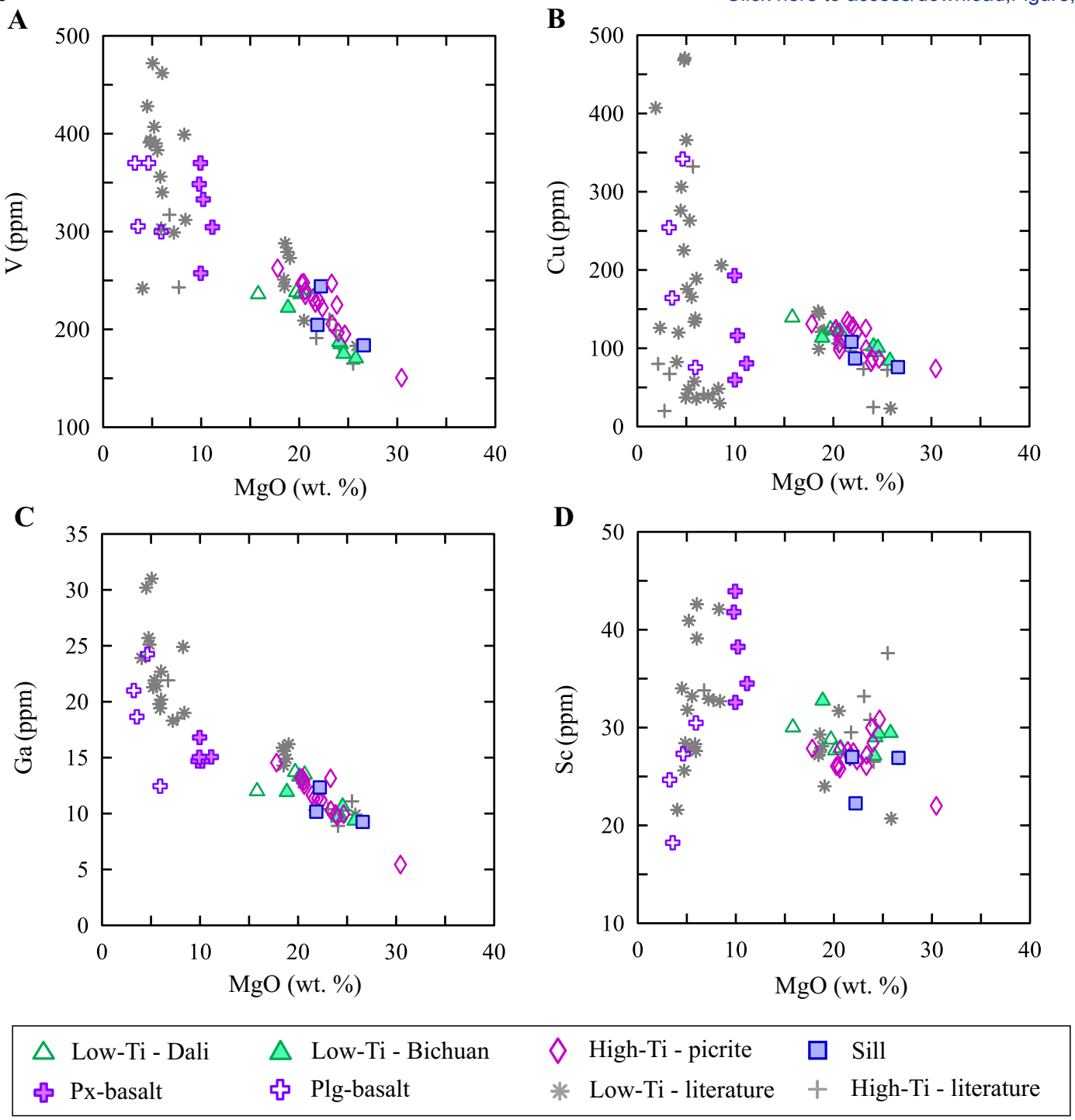

Figure 7

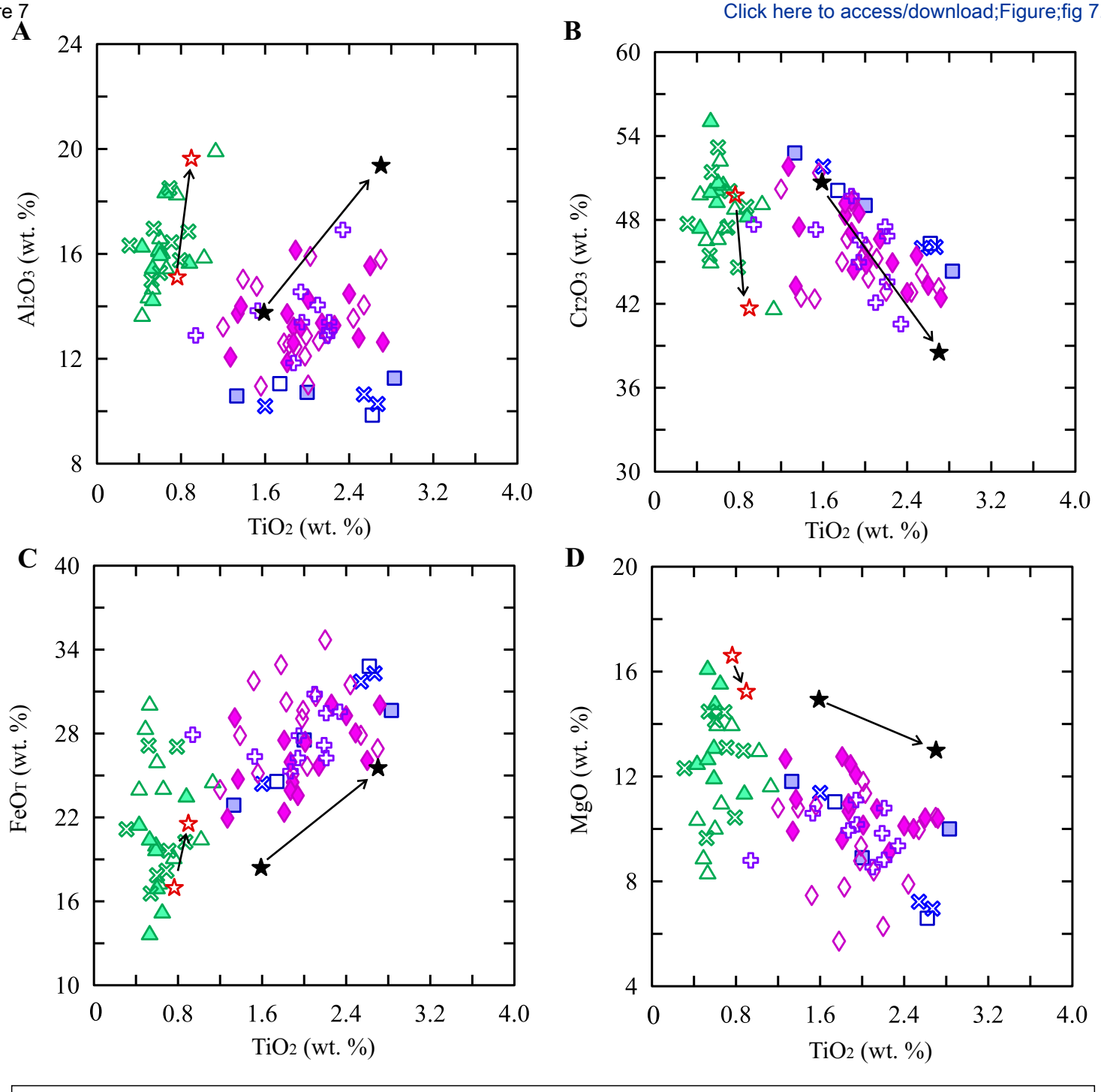

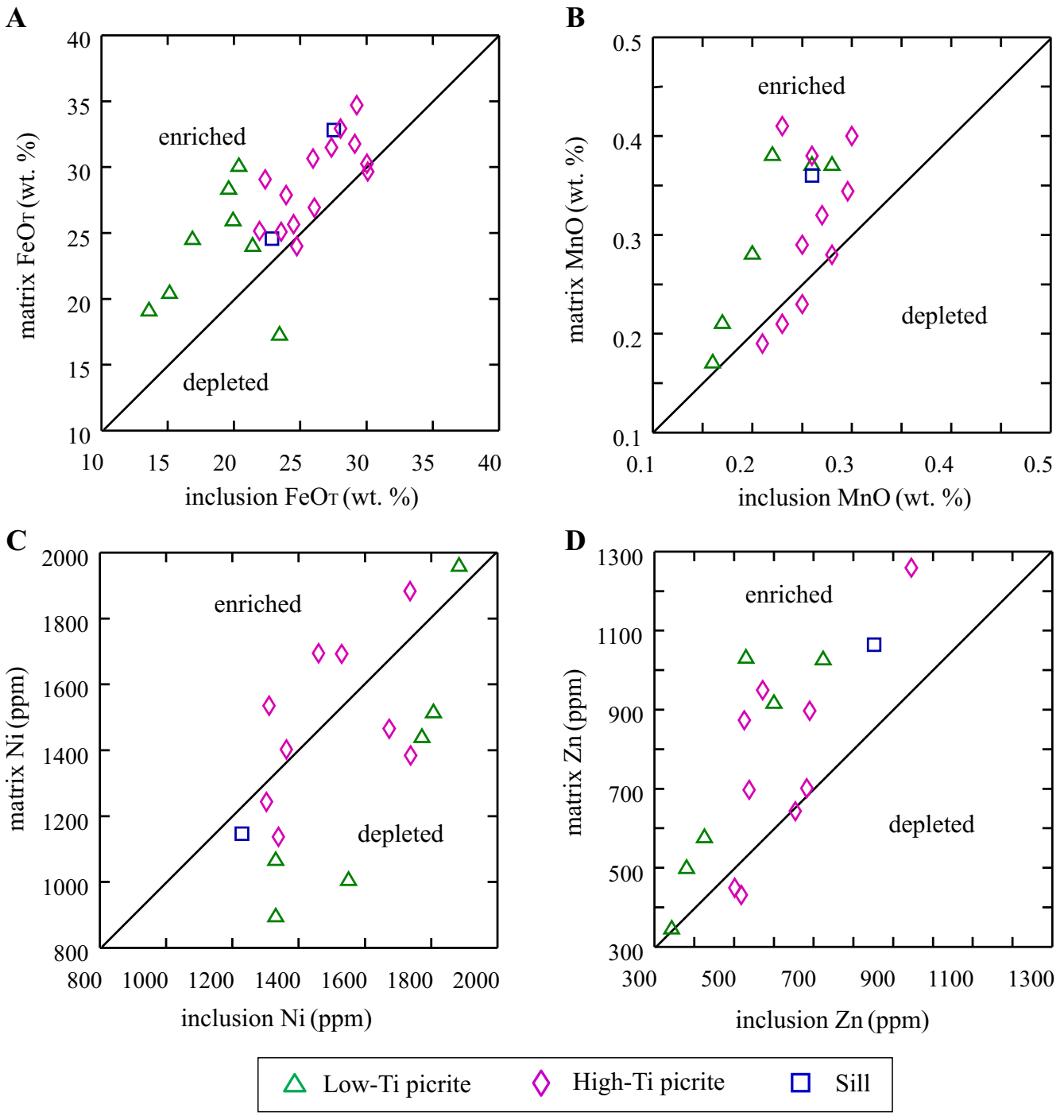

Fig. 8

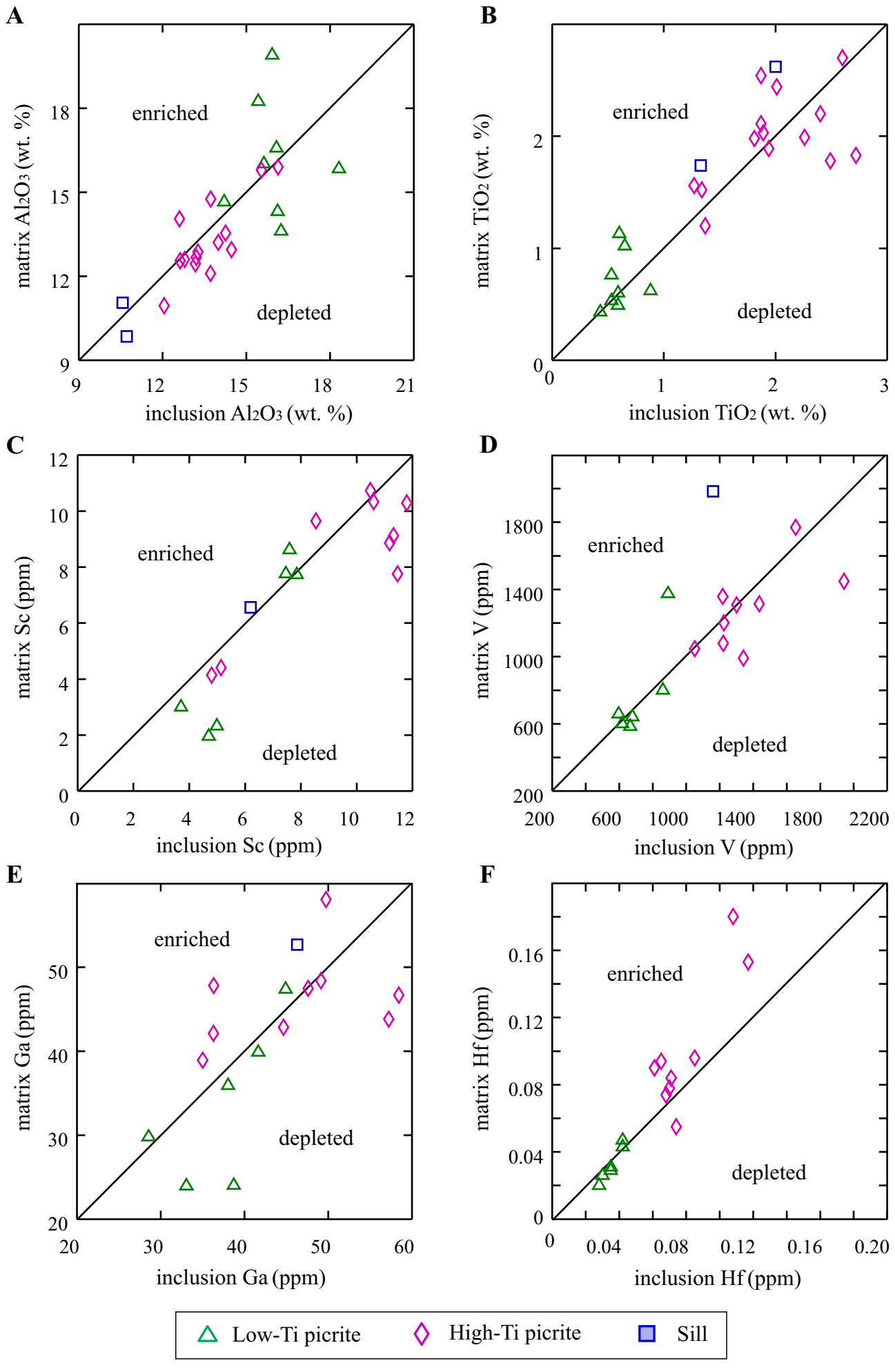

Figure 10

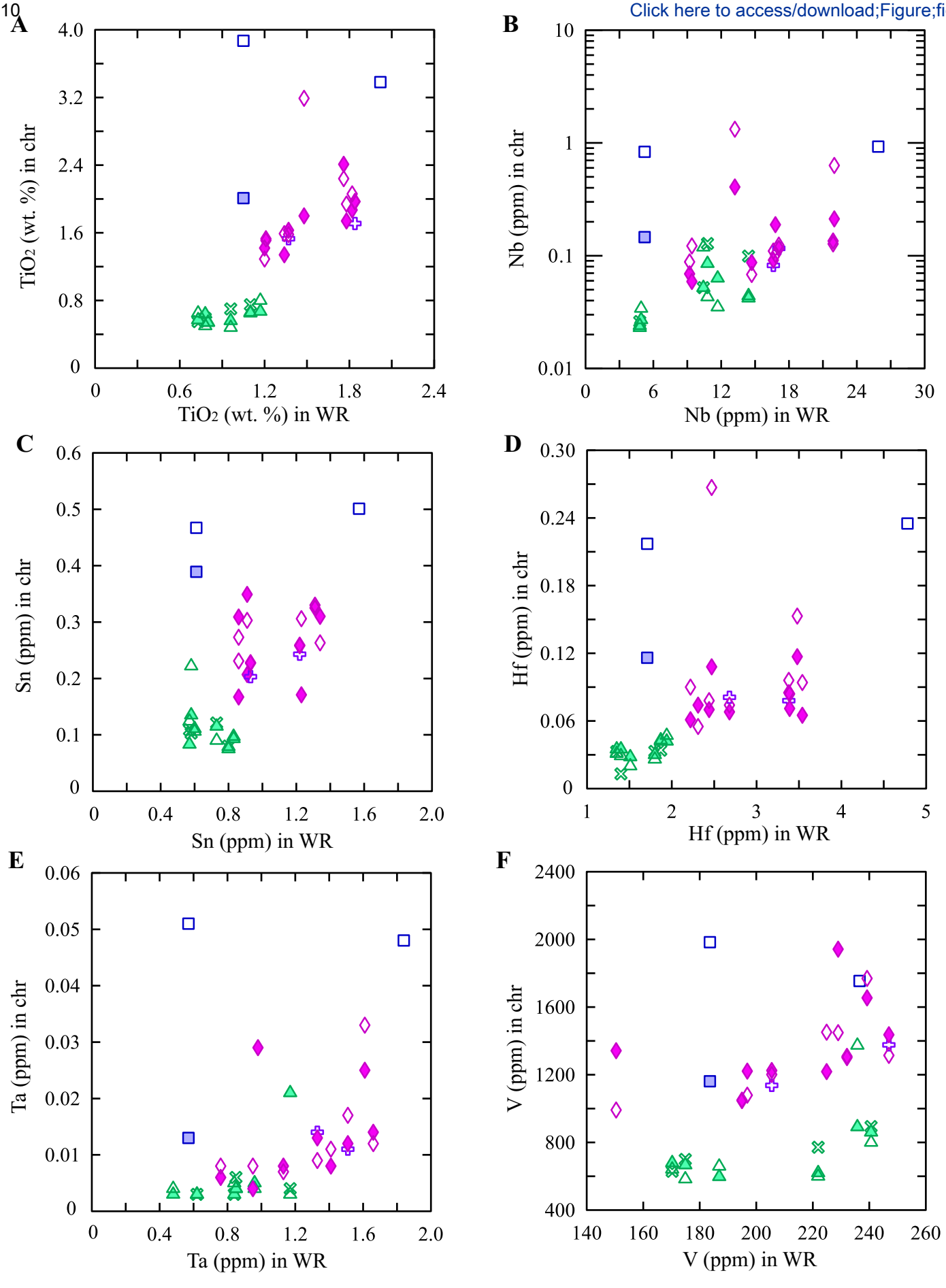

Figure 11

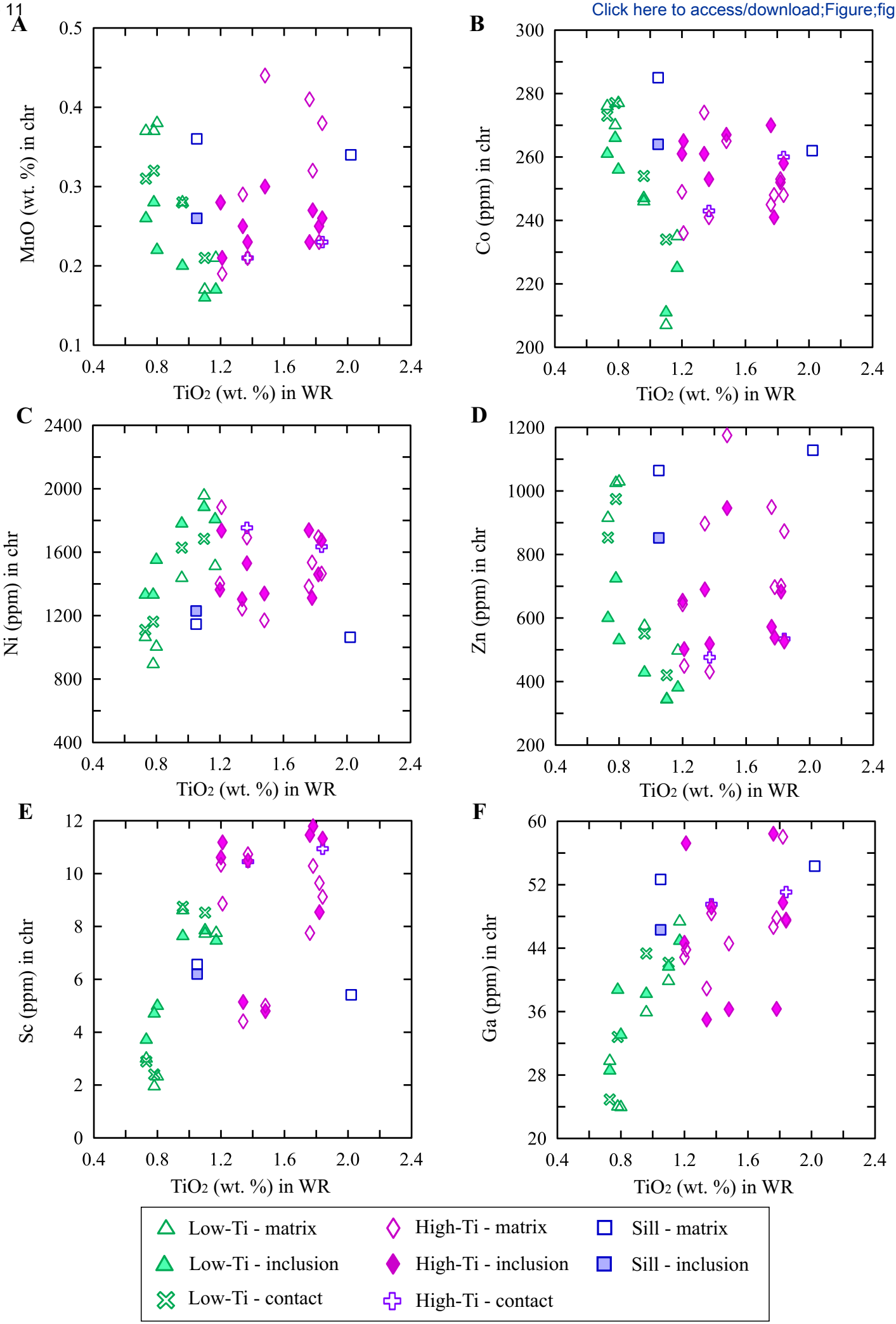

Figure 12

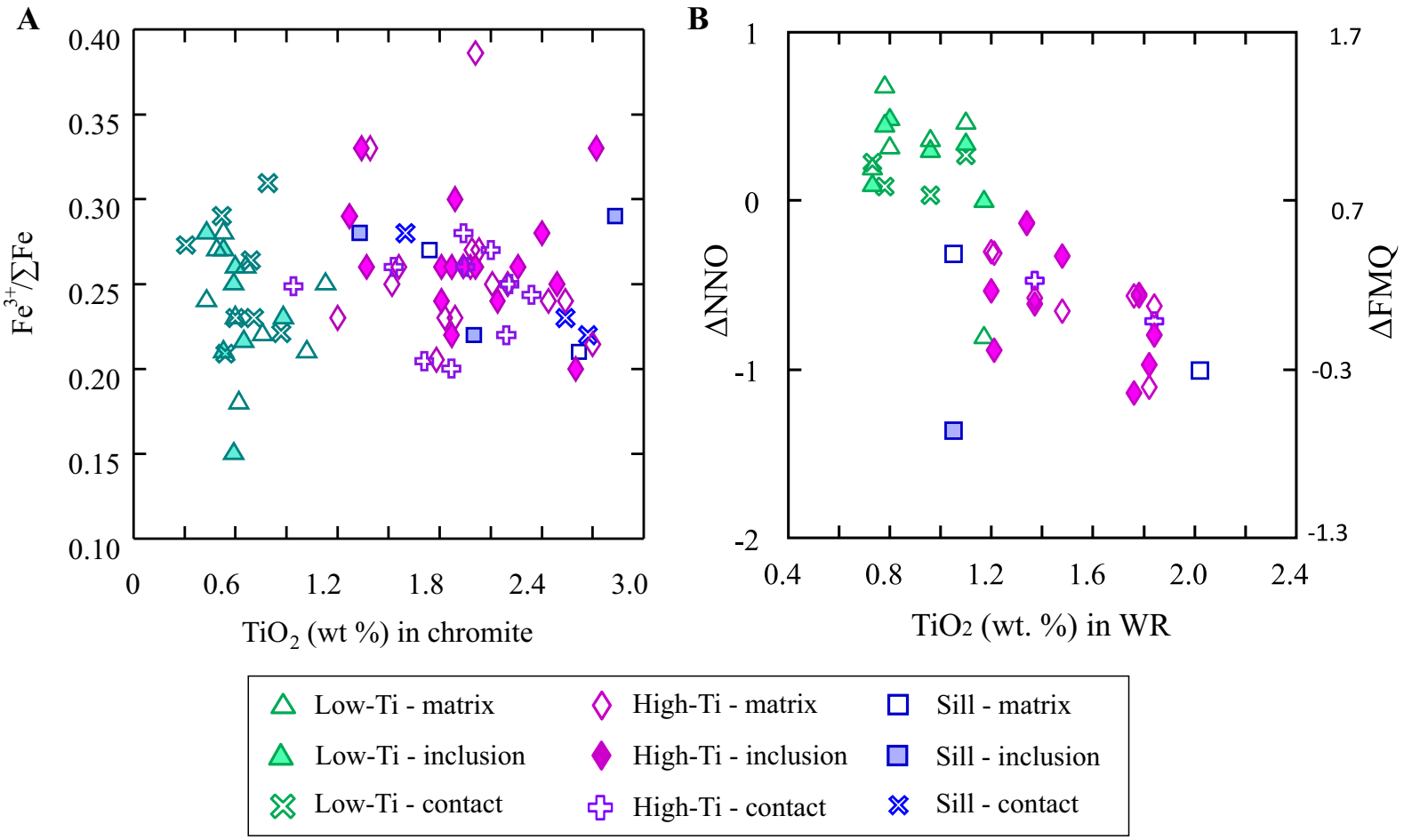

Figure 13

Click here to access/download;Figure;fig 13.pdf

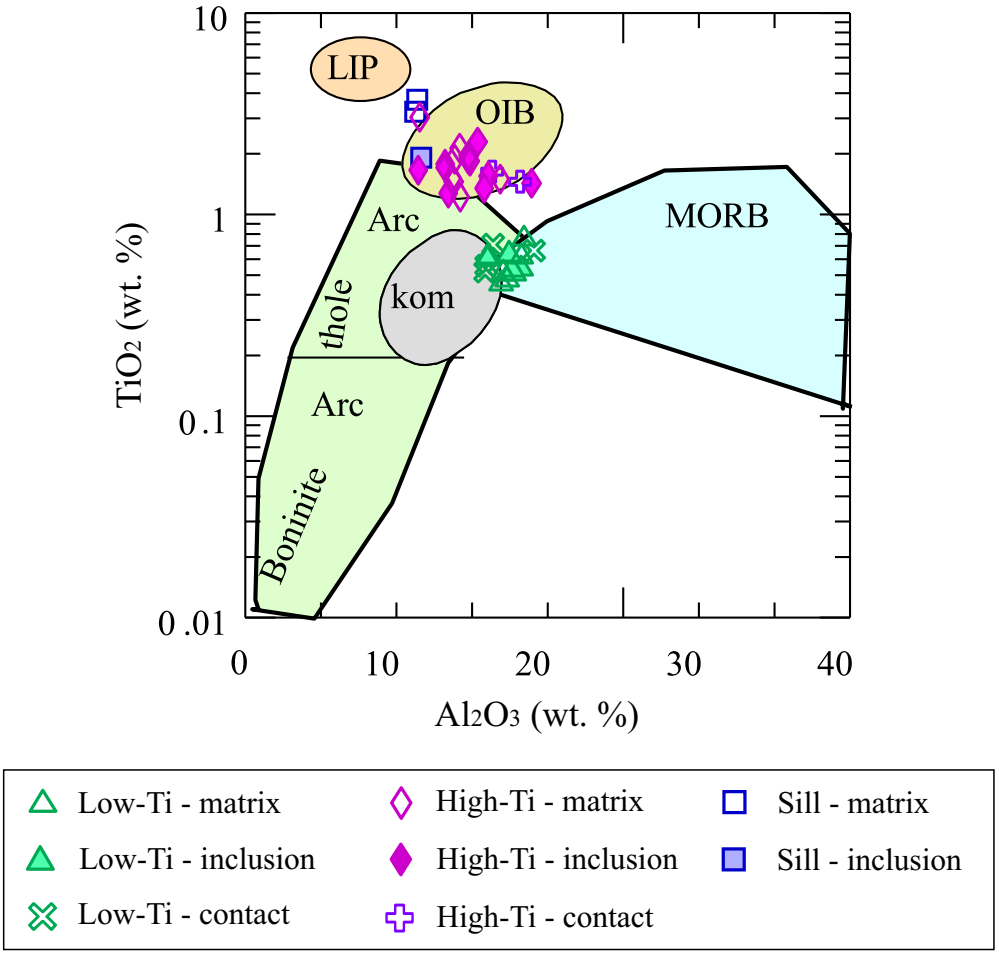

Figure 14

Click here to access/download;Figure;fig 14.pdf

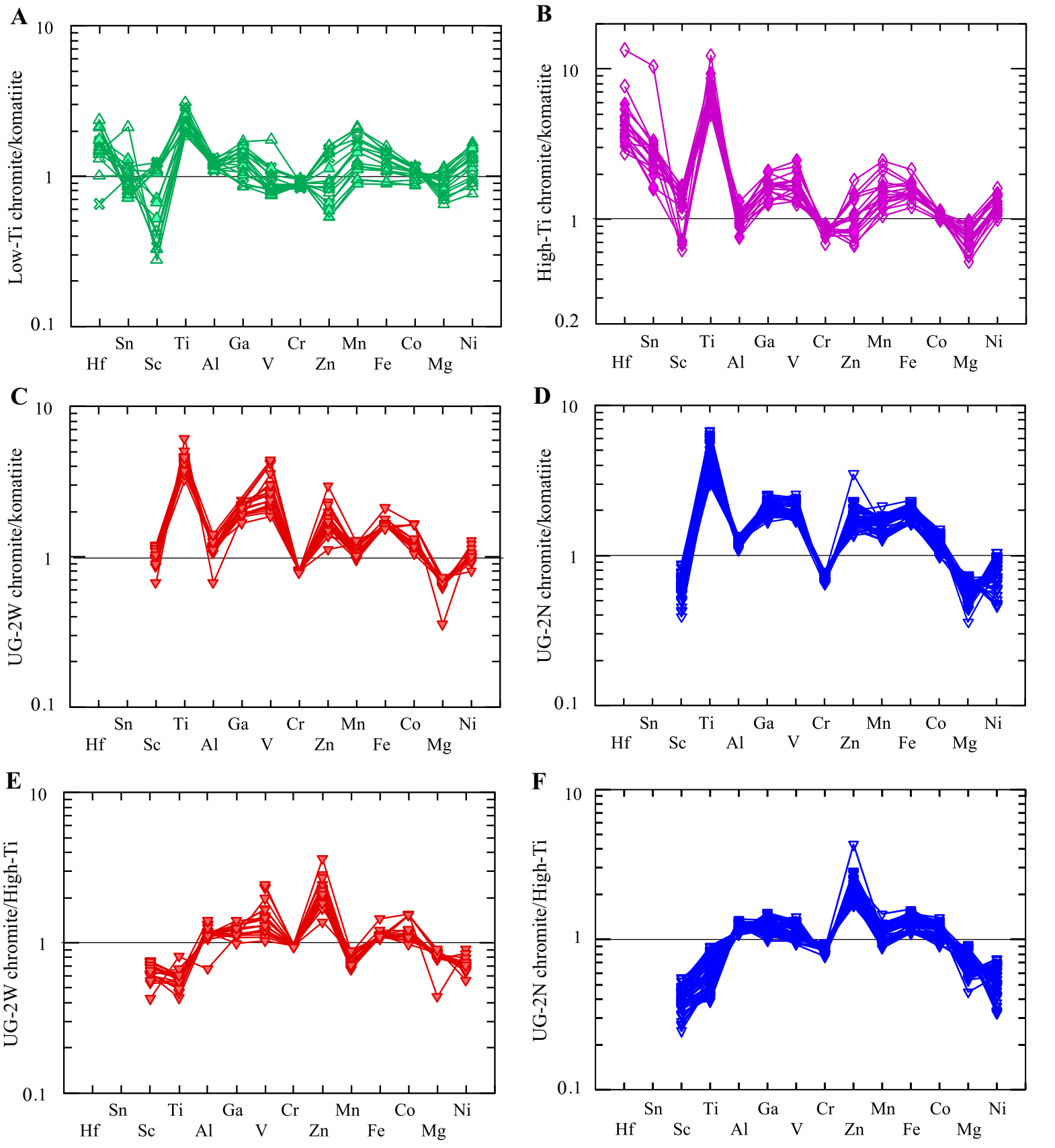

Table 1
Average Compositions Emeishan Picrites

	Low-Ti picrite	High-Ti picrite	Sill
n	9.00	15.00	3.00
SiO2 wt%	45.55	45.25	45.76
TiO2	0.95	1.64	1.71
Al2O3	9.42	8.15	6.43
FeOT	10.63	11.54	11.91
MnO	0.18	0.18	0.18
MgO	21.54	21.88	23.56
CaO	8.95	8.64	7.58
Na2O	1.10	0.86	0.65
K2O	0.31	0.36	0.71
P2O5	0.17	0.20	0.17
LOI	3.43	4.31	3.79
Ba ppm	197	169	243
Be	0.70	0.93	0.69
Cd	0.07	0.07	0.08
Ce	22.4	35.4	46.8
Co	96.0	97.0	101.7
Cr	1916	1937	2104
Cs	2.33	1.52	1.19
Cu	111	109	77
Dy	3.10	3.31	3.17
Er	1.69	1.64	1.38
Eu	1.00	1.32	1.62
Ga	11.5	11.2	11.3
Gd	3.18	3.87	4.39
Hf	1.67	3.02	3.74
Ho	0.61	0.61	0.54
In	0.05	0.05	0.05
La	10.9	16.0	20.6
Li	7.73	6.32	9.89
Lu	0.21	0.19	0.14
Mo	0.50	0.71	0.86
Nb	8.71	16.17	19.06
Nd	12.4	19.7	26.5
Ni	999	1000	1106
Pb	1.75	1.86	2.71
Pr	2.94	4.69	6.25
Rb	16.3	14.7	29.0
S	<40	150	69
Sb	0.04	0.05	0.06

Sc	29	27	24
Sm	2.96	4.15	5.36
Sn	0.70	1.11	1.19
Sr	205	198	283
Ta	0.81	1.31	1.43
Tb	0.50	0.57	0.59
Th	1.50	1.79	2.55
Tl	0.04	0.03	0.02
Tm	0.23	0.22	0.17
U	0.35	0.43	0.59
V	210	221	221
Y	16.1	16.0	13.9
Yb	1.43	1.32	1.01
Zn	78.9	85.8	89.8
Zr	64.4	120.8	149.0
Os ppb	1.46	2.07	4.20
Ir	0.96	1.28	1.87
Ru	2.08	2.18	3.58
Rh	0.57	0.50	0.68
Pt	7.82	8.41	17.81
Pd	6.17	4.76	7.92
Au	1.25	1.56	2.51

n = number of samples FeOT= total Fe

Table 2

Average Composition of Chromites as Determined by Microprobe analysis

Average	n	SiO_2 wt %	TiO_2 wt %	Al_2O_3 wt %	Cr_2O_3 wt %	FeOT wt %	MgO wt %	Total wt %
All	198	0.11	1.71	13.67	46.57	26.34	10.45	99.40
Hi-Ti Picrite All	122	0.09	2.04	13.32	45.50	27.82	10.02	99.37
inclusion	53	0.11	1.98	13.49	46.01	26.59	10.67	99.43
matrix	38	0.08	1.87	13.33	45.39	28.60	9.46	99.33
contact	31	0.08	2.32	13.00	44.76	28.98	9.58	99.34
Low-Ti Picrite All	51	0.14	0.64	16.05	48.63	21.35	12.34	99.64
inclusion	19	0.16	0.57	15.91	49.69	19.30	13.26	99.34
matrix	21	0.14	0.71	16.12	47.55	23.32	11.39	99.76
contact	11	0.14	0.64	16.05	48.63	21.35	12.34	99.64
Sill	25	0.15	2.30	10.55	47.59	29.25	8.71	99.09
inclusion	7	0.23	2.16	10.91	48.08	27.10	10.20	99.27
matrix	8	0.15	2.03	10.39	49.11	27.61	9.45	99.25
contact	10	0.10	2.62	10.42	46.02	32.05	7.06	98.83

		FeO [a]	Fe_2O_3 [a]	Mg# [b]	Cr# [c]	Fe^{3+}/FeT	stdev
All	198	19.89	7.17	48.79	69.63	0.2560	0.0438
Hi-Ti Picrite All	122	20.82	7.78	46.60	69.60	0.2639	0.0441
inclusion	53	19.85	7.49	49.45	69.56	0.2643	0.0473
matrix	38	21.45	7.95	44.36	69.51	0.2654	0.0443
contact	31	21.72	8.07	44.47	69.77	0.2609	0.0393
Low-Ti Picrite All	51	16.35	5.55	57.76	67.03	0.2369	0.0442
inclusion	19	14.78	5.02	62.04	67.69	0.2371	0.0540
matrix	21	17.97	5.95	53.42	66.47	0.2442	0.0381
contact	11	16.35	5.55	57.76	67.03	0.2520	0.0379
Sill	25	22.54	7.45	41.22	75.10	0.2443	0.0323
inclusion	7	20.33	7.53	47.94	74.61	0.2633	0.0385
matrix	8	21.17	7.16	44.73	76.02	0.2410	0.0354
contact	10	25.19	7.63	33.71	74.72	0.2349	0.0109

n=number of analyses FeOT=all Fe .

[a] FeO and Fe2O3 using Barnes and Roeder (2001; Journal of Petrology website)

[b] Mg# = 100 * [Mg] / ([Fe^{2+}] + [Mg]) [c] Cr# = 100 * [Cr] / ([Cr] + [Al]) [d] Fe^{3+}/FeT = [Fe^{3+}]/[Fe total].

Table 3

Average Chromite Compositions of Emeishan Chromites as Determined by LA-ICP-MS

	High-Ti picrite						***Low-Ti picrite***					
	All		Inclusions		Matrix		All		Inclusions		Matrix	
	average	stdev	average	stdev	average	stdev	average	stdev	average	stdev	average	stdev
n	89		29		57		59		21		31	
Al2O3 wt%	13.59	1.82	13.48	2.17	13.15	1.09	16.02	0.98	16.19	0.75	16.13	0.87
MgO	10.10	1.77	10.34	1.13	9.41	2.08	11.77	1.97	13.07	1.56	10.78	2.15
TiO2	1.78	0.33	1.74	0.33	1.84	0.37	0.61	0.09	0.60	0.06	0.60	0.12
Cr2O3	45.16	2.48	45.24	2.66	45.28	2.67	48.50	2.13	49.44	1.92	48.04	2.34
MnO	0.27	0.06	0.25	0.03	0.30	0.08	0.26	0.07	0.21	0.05	0.30	0.09
FeO T	27.28	4.13	26.85	2.14	28.40	5.56	21.73	3.75	19.82	3.35	22.79	4.47
Sc ppm	9.10	2.52	9.48	2.73	8.36	2.49	5.64	2.61	6.05	1.79	5.22	3.11
V	1321	244	1377	271	1279	240	747	197	718	126	776	302
Co	255	11	259	9	252	13	251	23	244	22	252	28
Ni	1514	203	1495	181	1493	236	1445	333	1613	245	1311	401
Cu	91	100	84	103	111	108	85	67	73	62	93	83
Zn	677	212	625	141	766	260	637	248	501	145	731	296
Ga	46.55	6.83	46.04	8.78	46.22	5.43	35.56	7.66	37.49	5.90	33.47	9.31
Ge	3.25	0.43	3.22	0.28	3.39	0.51	2.59	0.40	2.43	0.48	2.67	0.42
Y	0.015	0.009	0.015	0.008	0.015	0.010	0.023	0.014	0.023	0.012	0.020	0.010
Nb	0.181	0.181	0.152	0.109	0.230	0.247	0.056	0.034	0.049	0.023	0.050	0.035
Mo	0.057	0.094	0.081	0.140	0.039	0.015	<0.035		<0.035		<0.035	
Ru	0.250	0.074	0.260	0.082	0.245	0.077	0.298	0.040	0.287	0.038	0.303	0.033
Rh	0.023	0.008	0.023	0.010	0.025	0.007	0.018	0.008	0.015	0.007	0.017	0.006
Pd	<0.017		<0.017		<0.017		<0.017		<0.017		<0.017	
Cd	<0.045		<0.045		<0.045		<0.045		<0.045		<0.045	
In	0.033	0.008	0.031	0.008	0.036	0.009	0.021	0.005	0.017	0.004	0.023	0.005
Sn	0.290	0.139	0.258	0.068	0.337	0.190	0.109	0.035	0.102	0.022	0.120	0.053
Hf	0.089	0.032	0.080	0.020	0.101	0.041	0.033	0.009	0.035	0.006	0.033	0.010
Ta	0.014	0.010	0.013	0.009	0.016	0.012	0.004	0.005	0.006	0.007	0.003	0.002
Re	<0.015		<0.015		<0.015		<0.015		<0.015		<0.015	
Os	0.042	0.014	0.042	0.012	0.044	0.016	0.037	0.008	0.036	0.008	0.037	0.007
Ir	0.036	0.032	0.047	0.045	0.028	0.016	0.031	0.011	0.036	0.016	0.025	0.008
Pt	<0.017		<0.017		<0.017		<0.017		<0.017		<0.017	
Au	<0.012		<0.012		<0.012		<0.012		<0.012		<0.012	
Bi	0.028	0.072	0.046	0.108	0.013	0.006	<0.009		<0.009		<0.009	

n=number of grains of each habit. Averages for contact grains not shown. FeOT = Total Fe.

LOD = Limit of detection Longerich et al. (1996) LOQ = Limit of quanitication 3.3*LOD

Table 3 (continued)

Average Chromite Compositions of Emeishan Chromites as Determined by LA-ICP-MS

	Sill					***All chromites***			
	All		Inclusions		Matrix			LOD	LOQ
	average	stdev	average	stdev	average	stdev	average	stdev		
n	18		4		14		166			
Al2O3 wt%	10.22	0.22	10.46		10.10	0.09	14.33	2.20	0.0001	0.0003
MgO	6.52	1.12	7.76		5.91	0.47	10.51	2.27	0.0001	0.0002
TiO2	3.09	0.97	2.01		3.63	0.34	1.40	0.82	0.0001	0.0003
Cr2O3	42.16	4.35	46.81		39.83	2.30	46.30	3.15	0.0001	0.0002
MnO	0.32	0.05	0.26		0.35	0.01	0.27	0.07	0.0001	0.0004
FeO T	34.37	3.92	29.95		36.58	1.24	25.55	5.36	0.0001	0.0003
Sc ppm	6.05	0.59	6.20		5.98	0.82	7.44	2.97	0.090	0.297
V	1633	424	1161		1868	162	1110	394	0.070	0.231
Co	270	13	264		273	16	254	17	0.068	0.225
Ni	1146	83	1229		1104	59	1457	272	0.228	0.753
Cu	66	26	40		79	17	86	83	0.213	0.703
Zn	1015	144	852		1096	45	686	240	0.288	0.951
Ga	51.11	4.23	46.31		53.50	1.18	42.39	9.07	0.017	0.055
Ge	4.90	1.74	3.54		5.58	1.82	3.11	0.83	0.297	0.982
Y	0.042	0.029	0.017		0.054	0.028	0.020	0.015	0.005	0.016
Nb	0.634	0.426	0.146		0.879	0.066	0.165	0.221	0.006	0.021
Mo	0.076	0.025	0.049		0.089	0.013	0.049	0.069	0.035	0.116
Ru	0.295	0.030	0.289		0.297	0.042	0.273	0.063	0.040	0.131
Rh	0.025	0.009	0.014		0.030	0.001	0.021	0.008	0.006	0.018
Pd	<0.017		<0.017		<0.017		<0.017		0.017	0.055
Cd	<0.045		<0.045		<0.045		<0.045		0.045	0.148
In	0.088	0.074	0.028		0.118	0.075	0.032	0.025	0.012	0.039
Sn	0.452	0.057	0.389		0.484	0.024	0.228	0.149	0.049	0.162
Hf	0.189	0.064	0.116		0.226	0.013	0.074	0.051	0.009	0.030
Ta	0.038	0.021	0.013		0.050	0.002	0.012	0.013	0.003	0.009
Re	<0.015		<0.015		<0.015		<0.015		0.015	0.050
Os	0.121	0.020	0.100		0.132	0.011	0.046	0.025	0.026	0.086
Ir	0.064	0.008	0.056		0.069	0.003	0.036	0.026	0.007	0.022
Pt	<0.017		<0.017		<0.017		<0.017		0.017	0.056
Au	<0.012		<0.012		<0.012		<0.012		0.012	0.040
Bi	<0.009		<0.009		<0.009		<0.009		0.009	0.029

n=number of grains of each habit. Averages for contact grains not shown. FeOT = Total Fe.

LOD = Limit of detection Longerich et al. (1996) LOQ = Limit of quanitication 3.3*LOD

Table 4

Range in Calculated Composition of the Melts

	Low-Ti BC-02 Most Mg	High-Ti JC-07 Most Mg	Low-Ti DL-03 Least Mg	High-Ti JC-05 Least Mg
SiO2 wt %	45.17	46.70	47.68	49.67
TiO2	0.93	2.22	1.51	2.63
Al2O3	10.05	10.31	13.45	12.94
FeOT	11.00	11.93	10.08	10.06
MnO	0.19	0.18	0.17	0.17
MgO	19.98	14.69	11.22	9.23
CaO	9.58	10.50	12.11	12.17
Na2O	1.21	1.36	1.58	1.78
K2O	0.38	0.33	0.34	0.31
P2O5	0.21	0.24	0.22	0.27
Ba ppm	297	168	78	185
Be	0.88	1.13	0.95	1.13
Cd	0.09	0.10	0.10	0.12
Ce	36.8	45.3	15.1	53.2
Co	101.0	93.0	93.8	86.2
Cr	1727	1001	801	294
Cs	4.12	5.77	2.97	3.84
Cu	110	151	166	175
Dy	3.27	4.65	4.56	5.67
Er	1.78	2.29	2.47	2.79
Eu	1.20	1.82	1.29	2.29
Ga	11.5	15.8	18.5	19.4
Gd	3.58	5.35	4.48	6.67
Hf	1.72	4.07	2.56	5.05
Ho	0.65	0.84	0.89	1.04
In	0.047	0.072	0.068	0.080
La	18.72	20.08	6.32	22.91
Li	9.19	6.08	13.01	4.64
Lu	0.22	0.25	0.30	0.32
Mo	0.60	1.12	0.71	1.40
Nb	13.7	20.6	6.6	22.7
Nd	17.9	26.4	11.6	31.7
Ni	797	563	344	225
Pb	2.53	1.86	1.86	2.05
Pr	4.56	6.16	2.32	7.29
Rb	20.6	18.2	26.1	22.1
S	<40	103.37	<40	85.44
Sb	0.05	0.06	0.05	0.07
Sc	33.72	31.39	38.19	37.13
Sm	3.63	5.80	3.62	6.84

Sn	0.73	1.47	1.10	1.95
Sr	380	313	193	403
Ta	1.06	1.82	0.85	2.08
Tb	0.55	0.80	0.73	0.97
Th	2.56	2.30	0.95	2.67
Tl	0.06	0.06	0.07	0.07
Tm	0.24	0.30	0.34	0.37
U	0.52	0.64	0.33	0.67
V	214	295	328	346
Y	16.8	22.3	23.5	27.4
Yb	1.51	1.78	2.11	2.20
Zn	74.8	90.3	85.2	86.8
Zr	70.1	162.7	94.5	202.7
Os ppb	2.12	2.77	1.12	0.47
Ir	1.24	1.84	0.74	0.59
Ru	2.05	1.95	0.97	0.69
Rh	0.57	0.52	0.42	0.37
Pt	8.30	10.88	11.15	11.13
Pd	7.15	10.54	9.86	10.69
Au	<0.45	3.28	2.04	3.49

Table 5

Estimation of Partition Coefficients Between Calculated Liquids and Chromites

	Chromites from High-Ti Picrite					Chromites from Low-Ti Picrite					Low-Ti	High-Ti	Literature Values		
	All	Matrix	stdev	Inclu	stdev	All	Matrix	stdev	Inclu	stdev	BC06	JC07			
n	20	9		9		16	6		6				Min	Max	Ref
Al	1.13	1.08	0.13	1.12	0.23	1.22	1.22	0.09	1.24	0.15	1.35	1.19	0.94	2.70	1,2,3,4
Cd	<0.5	<0.5		<0.5		<0.5	<0.5		<0.5		<0.5	<0.5			
Co	2.58	2.53	0.23	2.61	0.21	2.63	2.66	0.25	2.58	0.21	2.77	2.77	3.30	5.10	2,4,5
Cr	289	292	72	294	72	297	290	93	298	89	251	319	128	270	1,2,3,4
Cu	0.68	0.81	0.90	0.66	0.87	0.66	0.72	0.68	0.55	0.55	0.30	0.66	0.17	0.25	2
Fe	2.68	2.79	0.49	2.66	0.23	2.31	2.43	0.42	2.09	0.40	2.00	2.44	1.25	4.75	1,2,3,4
Ga	3.18	3.15	0.53	3.17	1.01	2.54	2.45	0.88	2.71	0.70	3.08	3.01	3.00	3.80	2,5
Hf	0.023	0.027	0.018	0.019	0.005	0.016	0.016	0.005	0.017	0.004	0.016	0.021	0.004	0.008	2
In	<0.5	<0.5		<0.5		<0.5	<0.5		<0.5		<0.5	<0.5			
Mg	0.76	0.71	0.11	0.79	0.11	0.89	0.83	0.34	0.99	0.30	0.76	0.72	1.00	2.09	1,2,3,4
Mn	1.50	1.67	0.39	1.39	0.15	1.52	1.73	0.45	1.26	0.39	1.12	1.42	0.70	1.53	1,2,3,4,5
Mo	<0.1	<0.1		<0.1		<0.1	<0.1		<0.1		<0.1	<0.1	0.009	0.013	2
Nb	0.010	0.014	0.021	0.007	0.006	0.005	0.004	0.003	0.004	0.002	0.003	0.006	0.001	0.002	2
Ni	4.54	4.57	2.25	4.68	2.63	2.77	2.43	1.33	2.98	1.21	2.60	2.98	5.00	18.60	1,2,5
Sc	0.24	0.22	0.08	0.25	0.09	0.16	0.15	0.10	0.17	0.08	0.22	0.36	0.13	0.30	2,4,5
Sn	0.21	0.25	0.22	0.17	0.05	0.13	0.14	0.06	0.12	0.04	0.15	0.18			
Ta	0.009	0.012	0.016	0.007	0.005	0.005	0.004	0.002	0.006	0.004	0.017	0.007	0.001	0.002	2
Ti	0.83	0.88	0.24	0.79	0.10	0.52	0.51	0.10	0.51	0.08	0.56	0.89	0.14	0.78	1,2,3,4,5
V	4.40	4.26	0.67	4.55	0.74	2.84	2.93	0.99	2.73	0.63	2.68	4.86	1.14	5.00	2,4,5
Y	<0.001	<0.001		<0.001		<0.001	<0.001		<0.001		<0.001	<0.001			
Zn	5.54	6.18	1.90	5.10	1.10	6.47	7.54	2.58	5.18	2.23	5.22	4.78	6.90	10.10	5

n=number of samples, Inclu= inclusion

References 1 Righer et al. (2004), 2 Wijbrans et al. (2015), 3 Brenan et al. (2012), 4 Horn et al. (1994), 5 Page and Barnes (2009)